



Tsunamis Generated by Submerged Landslides: Numerical Analysis of the Near-Field Wave Characteristics

A. Romano¹ , J. L. Lara² , G. Barajas² , B. Di Paolo² , G. Bellotti³ , M. Di Risio⁴ , I. J. Losada² , and P. De Girolamo¹

¹DICEA, Sapienza University of Rome, Rome, Italy, ²IHCantabria - Instituto de Hidráulica Ambiental, Universidad de Cantabria, Santander, Spain, ³Engineering Department, Roma Tre University, Rome, Italy, ⁴Department of Civil, Construction-Architectural and Environmental Engineering (DICEAA), Environmental and Maritime Hydraulic Laboratory (LIAM), L'Aquila University, L'Aquila, Italy

Key Points:

- A new 3-D numerical approach to model landslide-generated tsunamis with the overset mesh technique (OpenFOAM®) is presented and validated
- The related numerical study of the near-field waves, by varying the initial acceleration, highlights saturation in the tsunami generation
- A new relationship (“wavemaker curve”) to predict the near-field wave characteristics of landslide-generated tsunamis is proposed

Supporting Information:

- Supporting Information S1
- Data Set S1
- Data Set S2

Correspondence to:

A. Romano,
alessandro.romano@uniroma1.it

Citation:

Romano, A., Lara, J. L., Barajas, G., Di Paolo, B., Bellotti, G., Di Risio, M., et al. (2020). Tsunamis generated by submerged landslides: numerical analysis of the near-field wave characteristics. *Journal of Geophysical Research: Oceans*, 125, e2020JC016157. <https://doi.org/10.1029/2020JC016157>

Received 14 FEB 2020

Accepted 28 MAY 2020

Accepted article online 7 JUN 2020

Abstract The accurate modeling of the landslide-generated tsunami characteristics in the so-called near-field is crucial for many practical applications. In this paper, we present a new full-3-D numerical method for modeling tsunamis generated by rigid and impermeable landslides in OpenFOAM® based on the overset mesh technique. The approach has been successfully validated through the numerical reproduction of past experiments for landslide-generated tsunamis triggered by a rigid and impermeable wedge at a sloping coast. The method has been applied to perform a detailed numerical study of the near-field wave features induced by submerged landslides. A parametric analysis has been carried out to explore the importance of the landslide’s initial acceleration, directly related to the landslide-triggering mechanisms, on the tsunami generation process and on the related wave properties. Near-field analysis of the numerical results confirms that the influence of the initial acceleration on the tsunami wave properties is significant, affecting wave height, wave period, and wave celerity. Furthermore, it is found that the tsunami generation mechanism experiences a saturation effect for increasing landslide’s initial acceleration, confirming and extending previous studies. Moreover, the resulting extended database, composed of previous experimental data and new numerical ones, spanning a wider range of governing parameters, has been represented in the form of a “nondimensional wavemaker curve,” and a new relationship for predicting the wave properties in the near-field as a function of the Hammack number is proposed.

1. Introduction

Impulsive waves (i.e., tsunamis) can be generated by sudden displacements of volumes of water induced by earthquakes, landslides, volcanic eruptions, impacts of asteroids, and gradients of atmospheric pressure (Løvholt et al., 2015). Among these triggering mechanisms, landslides assume a relevant role, especially as far as confined geometries are concerned (e.g., bays, reservoirs, lakes, and fjords). Figure 1 shows two examples (left panel: Lituya Bay, Alaska; right panel: Stromboli Island, Italy) of areas prone to landslide tsunami hazard. The interest in landslide-generated tsunamis in proximity of the coast has risen in the last decades due to some devastating events, such as those in Lituya Bay in 1958 (Alaska, Fritz et al., 2009), in the Vajont Valley in 1963 (Italy, Panizzo et al., 2005), in Papua New Guinea in 1998 (Synolakis et al., 2002), in Stromboli in 2002 (Italy, Tinti et al., 2005), in Haiti in 2010 (Fritz et al., 2012), and recently in Indonesia in 2018 (Grilli et al., 2019).

The physical process at hand is generally characterized by different length and time scales than those of tsunamis generated by earthquakes. The triggering mechanism, i.e., the landslide, can be classified as subaerial, partially submerged, or completely submerged, depending on the initial landslide position (McFall & Fritz, 2016). When the landslide occurs directly at the water body boundary, the generated impulse waves radiate seaward and propagate alongshore. Since tsunami generation is likely to occur in shallow water regions, the interaction between the waves and the sloping sea bottom plays a relevant role. The waves can be refracted by the interaction with the bottom, and trapping mechanisms, like those typical for edge waves, can occur (Bellotti & Romano, 2017; Romano et al., 2013). The complex interaction that exists between the generation and propagation mechanisms is therefore to be carefully considered for a proper understanding of the generated wave features and, consequently, for developing effective tsunami early warning systems working in real time (e.g., Bellotti et al., 2009; Cecioni et al., 2011).



Figure 1. Left panel: aerial picture of Lituya Bay (Alaska, summer 1958; picture by D.J. Miller, United States Geological Survey) after the tsunami event. Right panel: front view of the Sciara del Fuoco at Stromboli Island (Southern Tyrrhenian Sea, Italy, summer 2019; picture by A. Romano) during a lava sliding event.

Landslide-generated tsunamis have been studied by experimental, analytical, and numerical modeling. As far as experimental models are concerned, a large variety of studies can be found in the scientific literature. These have been carried out by using both rigid and impermeable bodies (e.g., Di Risio, Bellotti, et al., 2009; Di Risio, De Girolamo, et al., 2009; Enet & Grilli, 2009b; Grilli & Watts, 2005; Liu et al., 2005; Romano et al., 2013, 2016; Watts, 1998, 2005) and deformable landslide models (e.g. Bullard et al., 2019; Fritz et al., 2004; Grilli et al., 2017; Heller & Hager, 2010; Lindström, 2016; McFall & Fritz, 2016; Miller et al., 2017; Mohammed & Fritz, 2012; Mulligan & Take, 2017; Viroulet et al., 2014; Zitti et al., 2016), of which effects, in terms of generated waves, have been investigated both in isolation and in combination (e.g., Heller & Spinneken, 2013; Tang et al., 2018). Moreover, 2-D and 3-D model configurations, studied either separately or combined (e.g., Heller & Spinneken, 2015), have been used to investigate a large variety of geometries (plane slopes, conical islands, reservoirs, etc.) and landslide types (subaerial, partially submerged, and completely submerged).

Experimental tests are often time and money consuming, especially if 3-D models are considered. Large facilities, as well as complex experimental configurations and sophisticated measurement systems, are often needed (see McFall & Fritz, 2016; Romano et al., 2016). Furthermore, it is not always possible to explore in detail the influence of all the involved parameters. In this sense, tsunamis generated by submerged landslides provide a good example. Often, the waves generated by submerged landslides are too small to get reliable measurements in the experimental facilities. Moreover, it can be difficult to explore the influence of a key governing parameter such as the initial acceleration a_0 . This parameter is commonly recognized to be a crucial one in the slide kinematics, in particular in the initial phase, when the energy transfer between the landslide and the water takes place. Indeed, a_0 is directly related to the triggering mechanisms of the landslide and governs the key parameters of the tsunami source (Enet & Grilli, 2007; Grilli et al., 2009; Kim et al., 2019; Løvholt et al., 2015; Najafi-Jilani & Ataie-Ashtiani, 2008; Romano et al., 2017; Watts, 1998; Watts et al., 2005). Several experimental studies explored the importance of a_0 by means of different techniques. Watts (1998) changed the landslide's density to obtain different values of a_0 . More recently, Romano et al. (2017) used a mechanical system controlled by an electric motor to change the kinematics of the landslide. Nevertheless, physical restrictions are inevitable, hindering the exploration of a wider range of cases (i.e., different landslide-triggering mechanisms).

In this sense, numerical modeling can provide a valuable complementation. Indeed, numerical modeling techniques have progressively supported physical ones in shedding light on the complex physical phenomena involved in the generation and propagation mechanisms of landslide-generated tsunamis. Similarly to experimental models, a multitude of approaches has been adopted during recent years for numerically modeling landslide-generated tsunamis (an extensive review has been provided by Yavari-Ramshe & Ataie-Ashtiani, 2016). Eulerian and Lagrangian frameworks with three grid types (structured, unstructured, and meshless) have been used for tsunami simulations, employing both depth-averaged models, using Nonlinear Shallow Water or Boussinesq equations, and Navier-Stokes models, considering both 2-D and

3-D configurations (e.g., Abadie et al., 2010, 2012; Bellotti et al., 2008; Clous & Abadie, 2019; Grilli et al., 2017; Heidarzadeh et al., 2020; Heller et al., 2016; Kim et al., 2019; Liu et al., 2005; Løvholt et al., 2005; Lynett & Liu, 2005; Montagna et al., 2011; Ruffini et al., 2019; Shi et al., 2016, 2018; Watts et al., 2003; Whittaker et al., 2017).

The most recently developed tools offered by computational fluid dynamics (CFD) can provide a significant support for shedding light on many of the unresolved aspects. In particular, they can be very useful to model the near-field wave characteristics induced by submerged landslides, exploring the influence of the landslide-triggering mechanisms in terms of the generated waves. Indeed, the accurate reproduction of the momentum exchange between the landslide and the water body, guaranteed by the CFD methods, is crucial for a detailed modeling of tsunami generation, propagation, and the interaction with the coastline.

In this paper, a numerical study of the near-field wave characteristics of tsunamis generated by submerged landslides is presented. To this end, we used a new method for numerically modeling tsunamis generated by rigid and impermeable submerged landslides with OpenFOAM® (v1812) by using an approach based on the overset mesh technique. The overset mesh method is newly introduced in the coastal engineering field. This technique has been successfully used to model the dynamics of floating bodies under the effects of waves and currents (e.g., Di Paolo et al., 2018) and other hydrodynamics problems (Chen, Qian, et al., 2019). The overset mesh is based on the use of two (or more) domains. The outer one (i.e., background domain) allows the motion of one, or more, inner domain(s) (i.e., moving domain) that contains a rigid body. The mutual exchange of information between the two domains is achieved by interpolation. The advantage of this approach, if compared with other methods available to simulate the interaction between a moving body and one or more fluids in OpenFOAM®, for example, the immersed boundary method (Chen, Heller, et al., 2019; Jasak et al., 2014), is that the resolution around the moving body is extremely accurate (i.e., body-fitted approach) and, which is even more important, remains constant throughout the simulation.

The modeling of the solid boundaries on which the landslide moves is another point of novelty of the present approach. The numerical reproduction of a body moving close to an impermeable surface is not possible by using the overset mesh method because of the mentioned interpolation procedure. Indeed, few computational cells are needed between the body and the domain's edges. In order to overcome this requirement of the method, the solid bodies, on which the landslide body moves, are modeled as a porous media with a very low permeability by using the VARANS approach proposed by del Jesus et al. (2012), Lara et al. (2012), and Losada et al. (2016). In order to validate the proposed approach against experimental data, the numerical reproduction of the experimental benchmark described by Liu et al. (2005) for landslide-generated tsunamis triggered by a rigid and impermeable wedge at a sloping coast has been carried out.

The validated numerical method has further been applied to a detailed study of the near-field wave features induced by submerged landslides. Parametric simulations, by varying the initial acceleration a_0 , have been carried out to explore the importance of this parameter on the tsunami generation process and on the related wave characteristics. The quantitative spatial analysis carried out in the near-field points out the significant influence of the initial acceleration on the tsunami wave features, also showing that “saturation” mechanisms (i.e., no more energy can be effectively transferred from the landslide to the water to generate larger waves) may occur for increasing values of the initial acceleration, confirming and extending the previous theoretical findings of Tinti and Bortolucci (2000). Furthermore, the new numerical results have been represented, together with experimental data from past works dealing with different landslide geometries and configurations, in the form of a “nondimensional wavemaker curve” (Watts, 1998). The excellent agreement between the previous experimental data and the numerical ones, involving wide parameter ranges, allowed to propose a new relationship for predicting the wave characteristics in the near field, induced by rigid and impermeable submerged landslides, as a function of the Hammack number.

The paper is structured as follows. After this introduction, the description of the numerical method is provided in section 2, while the validation of the method itself against experimental results is given in section 3. Sections 4 and 5 show the application of the proposed approach to investigate the features of the tsunami wave pattern induced by landslide-generated tsunamis in the near field. Finally, section 6 with the concluding remarks closes the paper.

2. Numerical Model

The new approach for numerically modeling tsunamis generated by rigid and impermeable landslides, described in this paper, has been developed on the OpenFOAM® platform (Jasak, 1996). IHFOAM (Higuera et al., 2013a, 2013b), based on interFoam of OpenFOAM®, includes wave boundary conditions and porous media solvers for coastal and offshore engineering applications and can solve both 3-D Reynolds-Averaged Navier-Stokes equations (RANS) and Volume-Averaged RANS equations (VARANS) for two phase flows. In the present work both RANS and VARANS equations have been used, and solved, coupled to the Volume of Fluid (VOF) equation and to the overset mesh method. In this section the base equations as well as a description of the proposed method are presented.

2.1. Governing Equations

The RANS equations, which allow to model the flow at the clear fluid region, are based on the Reynolds decomposition, which identifies an average and a fluctuating component (i.e., velocity and pressure fields for incompressible models). These equations are represented by the mass and momentum conservation equations, coupled to the VOF equation as follows:

$$\frac{\partial u_i}{\partial x_i} = 0, \quad (1)$$

$$\frac{\partial \rho u_i}{\partial t} + u_j \frac{\partial \rho u_i}{\partial x_j} = -g_j x_j \frac{\partial \rho}{\partial x_i} - \frac{\partial p^*}{\partial x_i} - f_{\sigma i} - \frac{\partial}{\partial x_j} \mu_{\text{eff}} \left(\frac{\partial \rho u_i}{\partial x_j} + \frac{\partial \rho u_j}{\partial x_i} \right), \quad (2)$$

$$\frac{\partial \alpha}{\partial t} + \frac{\partial u_i \alpha}{\partial x_i} + \frac{\partial u_{ci} \alpha (1 - \alpha)}{\partial x_i} = 0, \quad (3)$$

where u_i (m/s) are the ensemble averaged components of the velocity, x_i (m) the Cartesian coordinates, g_j (m/s^2) the components of the gravitational acceleration, ρ (kg/m^3) the density of the fluid, p^* the ensemble averaged pressure in excess of hydrostatic, defined as $p^* = p - \rho g_j x_j$ (Pa), being p the total pressure, α (-) the volume fraction (VOF indicator function), which is assumed to be 1 for the water phase and 0 for the air phase, and $f_{\sigma i}$ (N/m^3) the surface tension, defined as $f_{\sigma i} = \sigma \kappa \frac{\partial \alpha}{\partial x_i}$, where σ (N/m) is the surface tension constant and κ (1/m) the curvature (Brackbill et al., 1992). μ_{eff} ($\text{Pa} \cdot \text{s}$) is the effective dynamic viscosity that is defined as $\mu_{\text{eff}} = \mu + \rho \nu_t$ and takes into account the dynamic molecular (μ) and the turbulent viscosity effects ($\rho \nu_t$); ν_t (m^2/s) is the eddy viscosity, which is provided by the turbulence closure model. Finally,

the compression velocity u_{ci} (m/s) is calculated as $u_{ci} = \min[c_\alpha |u_i|, \max(|u_i|) \frac{\frac{\partial \alpha}{\partial x_i}}{\left| \frac{\partial \alpha}{\partial x_i} \right|}]$, where the compression

coefficient c_α (-) is assumed to be 1 (Marschall et al., 2012; Weller, 2008).

The VARANS equations allow to model the flow inside an eventual porous material, which is modeled as a continuous media. As shown in the following, additional terms are considered in the momentum equation to account for frictional forces exerted by the porous media. The mass and the momentum conservation equations, coupled to the VOF equation, read as follows:

$$\frac{\partial \bar{u}_i}{\partial x_i n} = 0, \quad (4)$$

$$(1 + c) \frac{\partial \rho \bar{u}_i}{\partial t n} + \frac{\bar{u}_j}{n} \frac{\partial \rho \bar{u}_i}{\partial x_j n} = -g_j x_j \frac{\partial \rho}{\partial x_i} - \frac{\partial p^*}{\partial x_i} - f_{\sigma i} - \frac{\partial}{\partial x_j} \mu_{\text{eff}} \left(\frac{\partial \rho \bar{u}_i}{\partial x_j n} + \frac{\partial \rho \bar{u}_j}{\partial x_i n} \right) + -A \bar{u}_i - B |\bar{u}_i| \bar{u}_i, \quad (5)$$

$$\frac{\partial \alpha}{\partial t} + \frac{\partial \bar{u}_i \alpha}{\partial x_i n} + \frac{\partial \bar{u}_{ci} \alpha (1 - \alpha)}{\partial x_i n} = 0, \quad (6)$$

where \bar{u}_i (m/s) are the volume averaged ensemble averaged velocity (or Darcy velocity) components, defined as $\bar{u}_i = \frac{1}{V_f} \int_{V_f} u_i dV$, being V_f (m^3) the fluid volume contained in the averaging volume V , n (-) is the porosity,

defined as the volume of voids over the total volume, and \bar{p}^* (Pa) the volume averaged ensemble averaged pressure in excess of hydrostatic defined as $p^* = \frac{1}{V_f} \int_{\partial V_f} p^* dS$ (see del Jesus et al., 2012). The coefficient A (–) takes into account the frictional force induced by laminar Darcy-type flow, B (–) accounts for the frictional force induced under turbulent flow conditions, and c (–) considers the added mass. Following the work of Engelund (1953), modified by Van Gent (1995), the expressions for A , B , and c are as follows:

$$A = a \frac{(1-n)^2 \mu}{n^3 D_{50}^2}, \quad (7)$$

$$B = b \left(1 + \frac{7.5}{KC} \right) \frac{(1-n) \rho}{n^3 D_{50}}, \quad (8)$$

$$c = \gamma \frac{1-n}{n}, \quad (9)$$

where D_{50} (m) is the mean nominal diameter of the porous material, KC (–) the Keulegan-Carpenter number, a (–) and b (–) are empirical nondimensional coefficients (see Lara et al., 2011; Losada et al., 2016) and $\gamma = 0.34$ (–) is a nondimensional parameter as proposed by Van Gent (1995).

These equations have been implemented in a solver within the OpenFOAM® framework by Higuera et al. (2014a, 2014b). The solver works as follows: At the clear fluid region (i.e., outside the porous region) the frictional forces exerted by the porous media are deleted (i.e., $a = b = c = 0$) and $n = 1$; thus, the VARANS are replaced by the RANS; inside the porous region the empirical coefficients, the parameters and the porosity related to the porous media (i.e., a , b , c , D_{50} , KC , and n) are defined; thus, the full set of VARANS is solved. It should be noted that the solver supports several turbulence models (e.g., two equation models, $k-\epsilon$, $k-\omega$, and $k-\omega-SST$). In this study, the $k-\epsilon$ turbulence model has been used.

Finally, it is worth noticing that the present formulation of the VARANS equations accounts for the spatial variation of the porous media properties (porosity gradient), thus differing from that proposed by Jensen et al. (2014). More details on the VARANS equations can be found in del Jesus et al. (2012), Lara et al. (2012), and Losada et al. (2016), while for a more thorough description of their implementation in OpenFOAM® we refer to Higuera et al. (2014a). In conclusion, the VARANS equations become RANS equations in a fluid region outside the porous medium when porosity becomes 1. Within the porous medium, porosity takes a value lower than 1, and then additional terms are activated in momentum equation to include, for example, the frictional forces induced by the porous medium or a decrement of mass and linear momentum.

2.2. Overset Mesh Method

In this subsection a brief description of the overset mesh framework (also known as Chimera or overlapping grids technique) is provided. To the knowledge of the authors, there are very few works that applied this promising technique for coastal and offshore engineering applications. This technique has mainly been used to simulate the dynamics of floating objects and the so-called water entry problem (e.g., Ma et al., 2018; Windt et al., 2018). More recently, Di Paolo et al. (2018) have applied this mesh technique to simulate the dynamics of floating bodies under the effects of waves and currents, while Chen, Qian, et al. (2019) have applied the Overset mesh method to reproduce a numerical wave tank for modeling free-surface hydrodynamic problems (e.g., water entry problem and dynamics of floating objects).

The overset mesh method is based on the use of two (or more) domains. The outer one (i.e., background domain) allows the motion of one, or more, inner domain(s) (i.e., moving domain) that contains a rigid body. Therefore, the two domains, which overlap each other, can be used to simulate a large variety of hydrodynamics applications, especially if large displacements are considered. The left panel of Figure 2 shows a sketch depicting the features of the method. The background domain and the moving one (blue hatching) are represented. Within the latter the rigid body (i.e., the landslide) is modeled as a rigid and impermeable object (red hatching). Furthermore, the same panel schematically represents the characteristics of the interaction between the two domains. The moving domain, containing the object, can move through the background one with six degrees of freedom. As stated, the two-way exchange of information between the

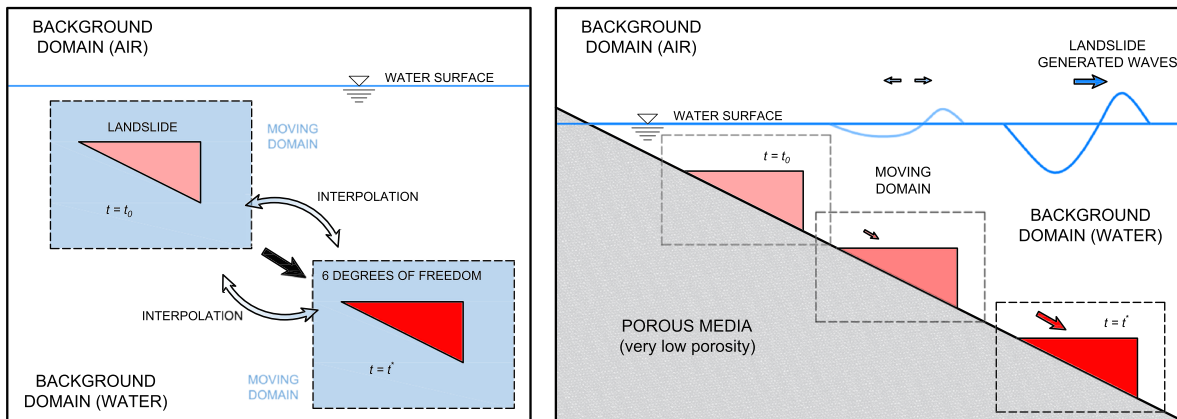


Figure 2. Left panel: sketch of the features of the overset mesh method. Right panel: sketch of the proposed approach for simulating landslide-tsunamis, that is, a sloping coast simulated as a porous media characterized by very low permeability.

background mesh and the moving one, to preserve continuity in the conservation of mass and linear momentum equations, requires interpolation of different scalar (pressure, density, turbulent kinetic energy, etc.) and vector fields (fluid velocity). The method followed to interpolate those magnitudes is the inverse distance method.

Conversely to other techniques (e.g., immersed boundary method or deforming mesh), this method offers the advantage that the resolution around the moving body is extremely accurate (i.e., body-fitted approach) and remains constant throughout the simulation. Thus, the strength of the overset mesh method lies in its ability to represent complex geometries while maintaining a good quality mesh, especially for large amplitude body motions (Chen, Qian, et al., 2019; Ma et al., 2018). This aspect is important for the momentum exchange between a rigid body and the water.

2.3. The New Approach for Landslide-Generated Tsunamis

All the features described in the sections 2.1 and 2.2 have been coupled for developing a numerical tool able to model tsunamis generated by rigid and impermeable landslides at a sloping coast. Indeed, although the overset mesh method seems to be suitable to address this task, the numerical modeling of a body, which is moving in contact with a solid and impermeable boundary (i.e., a sloping coast), is not possible yet because of the interpolation, on which the implementation is based. Indeed, few computational cells are needed between the body and the domain's boundaries. Obviously, this requirement of the overset mesh method does not affect the hydrodynamics modeling of floating bodies that are placed in the inner part of the numerical domain (i.e., far from the domain's boundaries), as shown in the cited works. Nevertheless, as far as landslide-generated tsunamis occurring at a sloping coast are concerned, for which the momentum transfer between the landslide and the water takes place during the sliding of the body along the inclined surface, this numerical implementation seems to be no longer an option.

In order to overcome this requirement of the overset mesh method we used an innovative approach to model the sloping coast along which the landslide moves. We modeled the sloping coast as a porous media characterized by a very low permeability (i.e., porosity $n < 0.01$) in order to simulate an impermeable surface, as shown in the right panel of Figure 2. This panel shows that the moving domain can be partly immersed in the porous media, completely matching the overset requirement without affecting the wave generation processes. Therefore, the sea bottom is not modeled as a solid boundary, instead it is just a part of the background domain in which a different set of equations (i.e., the VARANS equations valid for porous media flow) are solved. This approach allows the moving domain, which contains the landslide, to move through the background one and, consequently, the body to move by touching the sloping coast. Obviously, as discussed later, a preliminary tuning of the numerical parameters, which characterizes the porous media flow, is necessary to represent the sloping coast as close to an impermeable surface as possible.

To summarize, this approach is expected to be a powerful tool to model the phenomenon at hand (i.e., tsunamis generated by rigid and impermeable landslides), since, conversely to other techniques and implementations (e.g., cutting cells and immersed boundary method), it allows to resolve the boundary layer around complex 3-D geometries.

3. Validation Against Experimental Data

In order to validate the proposed approach and, consequently, to safely use the tool itself for the following parametric simulations, we reproduced numerically the experiments of Liu et al. (2005), valid for landslide-generated tsunamis triggered by a rigid and impermeable wedge at a sloping coast. The validation procedure is shown in this section.

3.1. Description of the Validation Case

A brief description of the experiments carried out by Liu et al. (2005) is given here, while the reader is referred to the original paper for more details. The large-scale experiments have been carried out in a 104.0-m long, 3.7-m wide, and 4.6-m deep wave tank by following Froude similarity laws. A plane slope, having an angle of inclination θ with the horizontal ($\tan\theta = 1/2$), was located near one end of the tank and a dissipating beach at the other end. For all experiments, the water depth in the wave tank was about 2.44 m. Liu et al. (2005) used several geometries (a wedge and a hemisphere) to represent the landslide; in this paper only the wedge has been considered.

The wedge-shaped slide has the following dimensions: length $b = 0.9144$ m, front face height $a = 0.4572$ m, and width $w = 0.6525$ m. Different initial slide positions have been used during their experiments, ranging from subaerial to submerged. Nevertheless, it is worth noticing that in the present paper only submerged landslides have been modeled. The slides moved down the slope by gravity, rolling on wheels. Figure 3 shows a definition sketch of the experimental setup as well as the nomenclature of the parameters used by Liu et al. (2005). The vertical distance between the still water level and the landslide's upper face is d , following the nomenclature shown in the upper right panel of Figure 3. The spatial coordinate x are measured as the seaward distance starting from the intersection of the SWL with the slope.

The runup and the free-surface elevation time series have been recorded with wave gauges. The free-surface elevation time series, measured along the centerline of the landslide by three wave gauges (WG1, WG2, and WG3), placed at $x_{WG1} = 1.796$ m, $x_{WG2} = 2.180$ m, and $x_{WG3} = 2.564$ m (see Figure 3) in a test with submerged landslide ($d/b = -0.33$), have been used as the validation case for our numerical approach.

3.2. Landslide Motion

To date, the numerical reproduction of the landslide kinematics, although a simple geometry and a rigid and impermeable landslide is considered, is not an easy task. The physical phenomena governing both the triggering and the evolution mechanisms of a landslide (submerged or subaerial) are far from being included in most of the numerical hydrodynamics codes, although some remarkable progresses have recently been achieved (e.g., Clous & Abadie, 2019; Shi et al., 2016; Si et al., 2018).

Additionally, the governing equation of landslide motion has been widely used in past studies (e.g., Romano et al., 2016, 2017), and, at least in the case of submerged landslides, analytical solutions are available (e.g., Pelinovsky & Poplavsky, 1996; Watts, 1998). Therefore, in this paper, we used the analytical solution provided by Pelinovsky and Poplavsky (1996), and later by Watts (1998), to reproduce the movement of the landslide, which has also been applied by Liu et al. (2005) to validate their large-eddy-simulations. The equation of motion of a sliding rigid body reads as follows:

$$(m + C_m m_0) \frac{d^2 s}{dt^2} = (m - m_0)g(\sin\theta - C_n \cos\theta) - \frac{1}{2} C_d \rho A \left(\frac{ds}{dt} \right)^2, \quad (10)$$

where m is the landslide mass, s the landslide displacement along the slope, t the elapsed time, g the gravitational acceleration, θ the incline slope angle, C_n the Coulomb friction coefficient, C_m the added mass coefficient, m_0 the displaced water mass, A the main cross section of the moving landslide (i.e., perpendicular to the direction of motion), ρ the water density, and C_d the global drag coefficient. In the case of submerged landslides the analytical solution of Equation 10, provided by Watts (1998), is

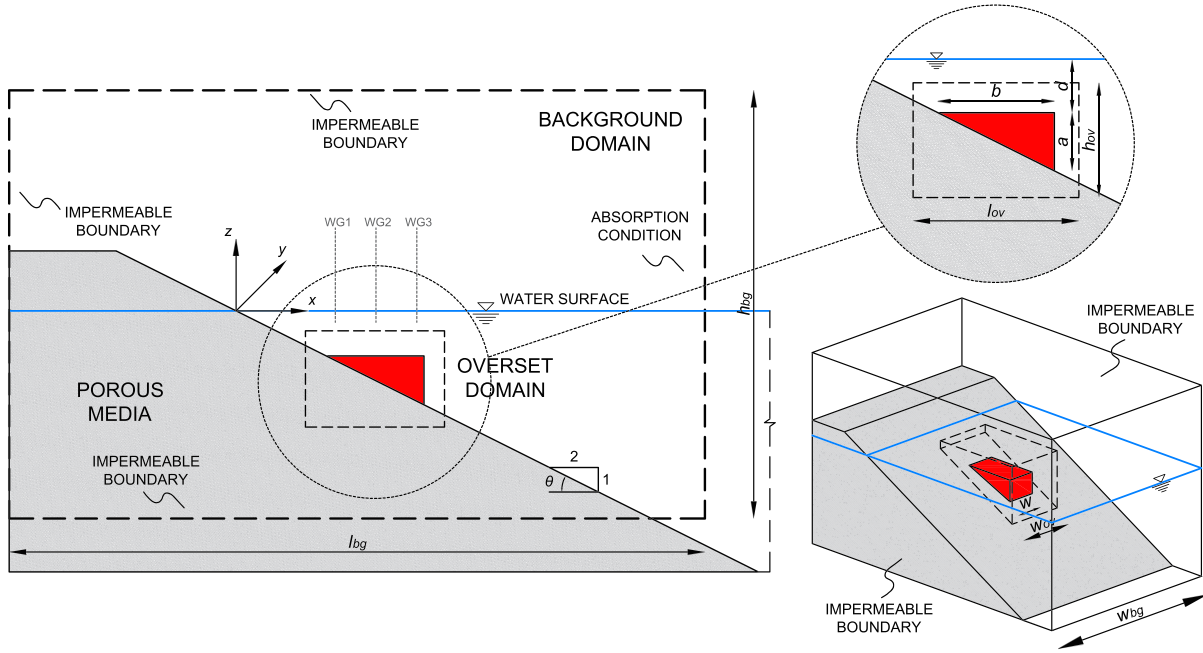


Figure 3. Left: side view of the experimental setup and numerical domains (background and moving). Right (upper panel): detail side view of the moving domain, dimensions of the landslide and nomenclature of the parameters. Right (lower panel): perspective view of the numerical domain. The boundary conditions are also specified.

$$s(t) = \frac{u_t^2}{a_0} \log \left[\cosh \left(\frac{a_0 t}{u_t} \right) \right], \quad (11)$$

$$u(t) = \frac{ds(t)}{dt} = u_t \tanh \left(\frac{a_0 t}{u_t} \right), \quad (12)$$

where a_0 is the initial acceleration and u_t is the terminal velocity that can be easily calculated as

$$a_0 = \frac{(m - m_0) g (\sin \theta - C_n \cos \theta)}{m + C_m m_0}, \quad (13)$$

$$u_t^2 = \frac{2(m - m_0) g (\sin \theta - C_n \cos \theta)}{C_d \rho A}, \quad (14)$$

once the hydrodynamics coefficients have been estimated. The left panel of Figure 4 shows the comparison between the analytical solution, used in this paper, and the experimental landslide motion from one of the experiments of Liu et al. (2005) that has been used for the validation of the new approach. In Figure 4 the red line refers to the analytical solution, while the black markers refer to the experimental data. Furthermore, the right panel of the figure shows the velocity of the body as obtained by Equation 10.

3.3. Numerical Setup

A numerical wave tank has been designed in order to reproduce the experiments of Liu et al. (2005). The numerical domain and the related boundary conditions are presented in Figure 3. According to the overset mesh method, a background domain and a moving one, containing the impermeable body (i.e., the landslide), have been defined. The background domain is 6.5 m long, 3.7 m wide and 4.0 m high, while the moving one is 1.3 m long, 1.1 m wide and 0.9 m high.

A preliminary grid refinement study has been carried out, following the approach described in Devolder et al. (2017). Three different mesh configurations, called coarse (C), medium (M), and fine (F), respectively, have been used for this purpose. The root mean-square error (RMSE) of free-surface elevation time series,

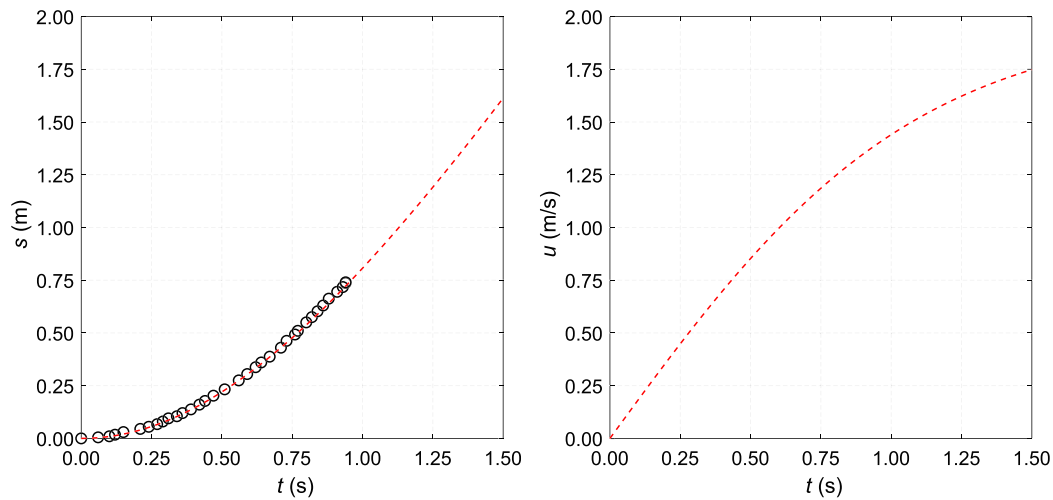


Figure 4. Left panel: analytical (red dashed line) and experimental (black circles) landslide motion as obtained by Liu et al. (2005). Right panel: analytical velocity time series of the landslide.

measured at WG3, has been used to quantify the discrepancies between experimental and numerical results. A summary of the mesh resolution, number of computational cells, computational time (CT), and RMSE, related to each preliminary case, is provided in Table 1.

The RMSEs related to the preliminary cases clearly show that the numerical results converge monotonically towards the experimental one. The mesh labeled Fine allows to obtain an $\text{RMSE} = 0.0013$ m, which is very small both in absolute and in relative (one order of magnitude smaller than the ones obtained with the two coarser meshes) value. On the other hand, this mesh is obviously very computationally expensive (more than 85 M of cells). In order to balance numerical model accuracy and computational cost, a new mesh, named Medium-Fine (M-F), has been created. The characteristics of this trade-off mesh are reported in Table 1. It can be seen that the RMSE for the Fine ($\text{RMSE} = 0.0013$ m) and Medium-Fine ($\text{RMSE} = 0.0031$ m) mesh configurations is in the same order of magnitude, testifying that a further refinement would only increase the CTs without leading to significant improvements of the results.

Thus, the chosen mesh (Medium-Fine) for the background domain is characterized by a cell resolution of 0.025 m along the x and y directions and 0.014 m along the z direction. In the moving domain the mesh is characterized by the same cell resolution as the background one, but the body-fitted approach ensures a much more detailed mesh resolution around the object (i.e., cell size in the order of few mm), which is placed in the center of the moving domain. The object has been modeled as a rigid and impermeable body. The geometrical dimensions of the landslide body are exactly the same of that used by Liu et al. (2005). The water depth h has been fixed to 2.44 m.

An active absorption boundary condition (Higuera et al., 2013a) has been applied at the right side on the numerical wave tank, while along the solid impermeable boundaries (lateral walls, left side, roof, and bottom) a no-slip velocity condition has been imposed. Furthermore, the plane slope (i.e., the sloping coast) along which the body slides has been modeled as a porous media characterized by a very low porosity (i.e., hydraulic conductivity $K < 9.0 \cdot 10^{-10}$ m/s). The moving domain (with the body contained in it) moves through the background domain according to Equation 11 as shown on the left panel of Figure 4.

3.4. Comparison with Experimental Data and Discussion of the Results

This validation focuses on the near field only. Thus, the numerical simulation has been stopped after 1.6 s from the beginning of the landslide's motion. Indeed, in this time window, the near-field wave features (i.e., first wave trough and first wave crest), evaluated by means of three free-surface elevation time series, are completely developed.

Figure 5 shows the comparison between numerical (red lines) and experimental (black dots) results for the three selected wave gauges. The three panels show the high degree of agreement between the two sets of data

Table 1
Case Name, Mesh Resolution, Number of Computational Cells, Computational Times (Hours per Seconds of Simulation per Processor Element) and RMSE of the Preliminary Numerical Cases

| Mesh | Object | | | Background | | | # cells | CT (h/s/PE) | RMSE (m) |
|------|-----------|-----------|-----------|------------|-----------|-----------|---------|-------------|----------|
| | D_x (m) | D_y (m) | D_z (m) | D_x (m) | D_y (m) | D_z (m) | | | |
| C | 0.03 | 0.05 | 0.04 | 0.065 | 0.074 | 0.06 | 0.53 M | 31.00 | 0.0213 |
| M | 0.029 | 0.029 | 0.03 | 0.05 | 0.052 | 0.029 | 1.13 M | 82.90 | 0.0112 |
| F | 0.01 | 0.01 | 0.003 | 0.015 | 0.015 | 0.005 | 85.21 M | 8320.00 | 0.0013 |
| M-F | 0.025 | 0.025 | 0.014 | 0.025 | 0.025 | 0.014 | 9.91 M | 995.52 | 0.0031 |

($RMSE\eta_{WG1} = 0.0010$ m, $RMSE\eta_{WG2} = 0.0027$ m and $RMSE\eta_{WG3} = 0.0031$ m). Starting from the upper panel, referring to the first wave gauge (η_{WG1}), it is evident that the numerical model is able to carefully reproduce the physics of such a complex physical phenomenon. As the submerged landslide starts to move, a small wave trough develops. A similar behavior is shown in the middle panel (η_{WG2}). Looking at the lower panel (η_{WG3}), the free-surface elevation time series firstly exhibits a wave trough followed by a wave crest, jointly induced by the rebound of the first wave trough and by the piston-like mechanism, which is a peculiar feature of the waves generated by submerged landslides. Moreover, Figure 6 shows a contour plot of the free-surface elevation, evaluated at four different time instants from the landslide release. Figure 6 enhances the good degree of symmetry of the numerical results throughout the simulation.

In order to validate the numerical approach only the available experimental measurements (i.e., free-surface elevation time series) have been used, but it is clear that the great advantage of using a full-3-D CFD tool, based on the Navier-Stokes equations, lies in having the full 3-D description (i.e., free-surface elevation,

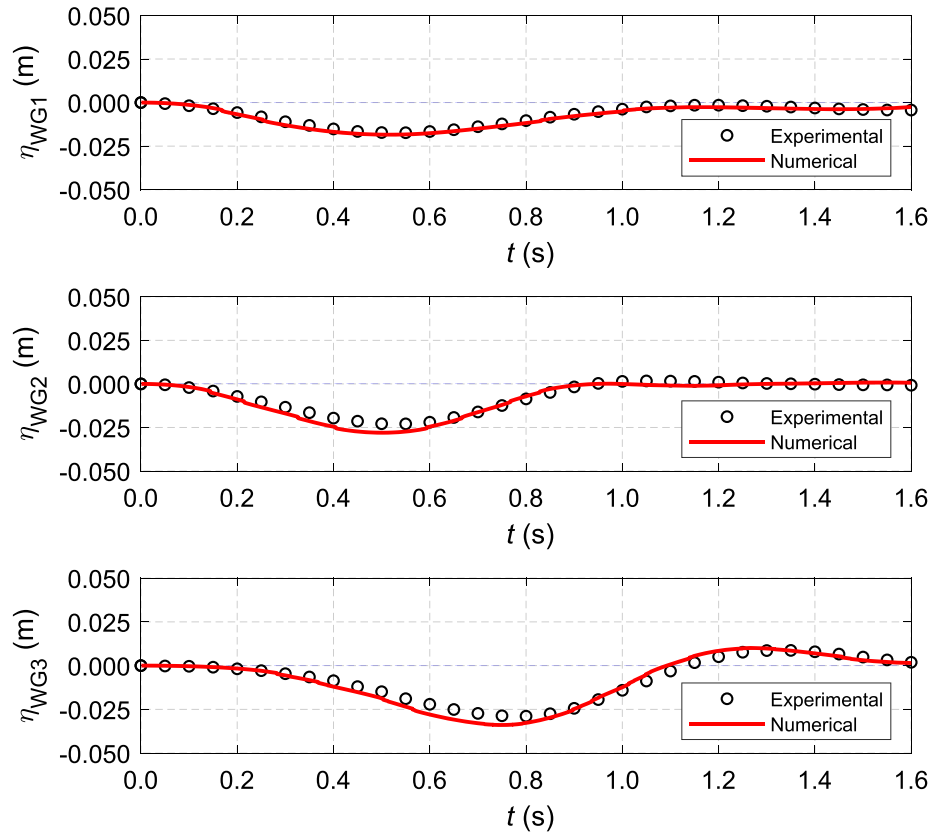


Figure 5. Comparison between experimental (black dots) and numerical (red lines) results, in terms of free-surface elevation time series, evaluated at the positions of the three wave gauges deployed by Liu et al. (2005).

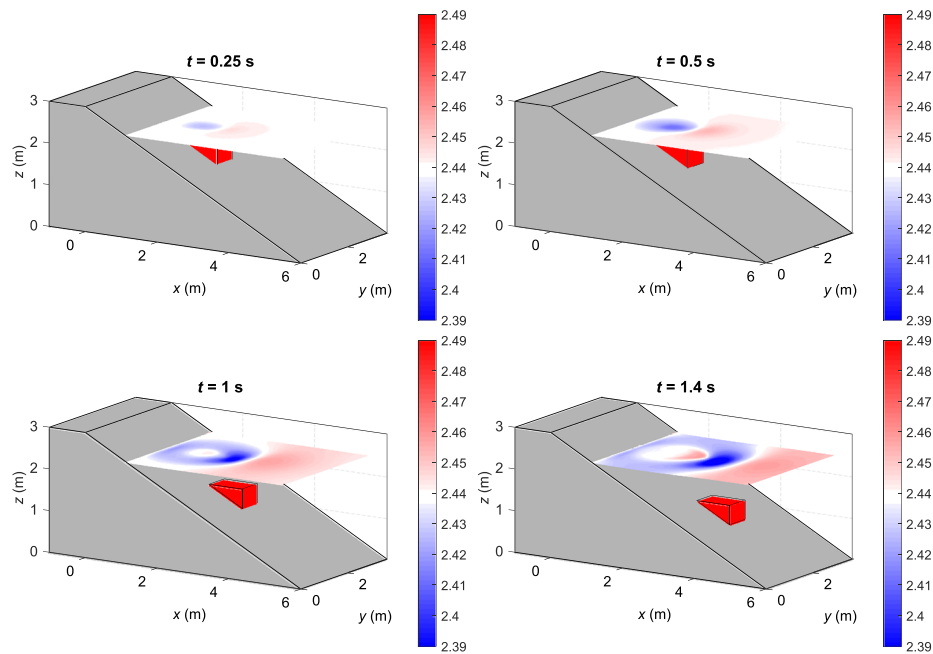


Figure 6. Contour plot of the free-surface elevation evaluated at four different time instants ($t = 0.25, 0.5, 1.0, 1.4$ s) after the landslide release.

velocity, and pressure field) of the phenomenon in the whole numerical domain, as shown in Figure 7. In this figure the velocity field, induced by the movement of the landslide at six selected time instants, is presented. Each row in Figure 7 refers to a different time instant, while in each column a given quantity, at the considered time step, is presented, namely, the first column shows the overset domain that, containing the landslide and embedded in the porous media, travels through the background one; the second and the third columns represent the contour plot and the vectorial diagram of the velocity field, respectively. Figure 7 shows the great potential of the numerical tool to describe the complex flow induced by landslide motion. Indeed, the velocity field accurately depicts the tsunami generation process. As the landslide starts to move the volume of water, placed above the moving body, points downward triggering the formation of the characteristic wave trough, while in front of the moving body the velocity field exhibits a horizontal component; thus, the landslide, pushing the water in front of it, triggers the piston-like mechanism that generates the leading wave crest that propagates seaward. Furthermore, a vortex structure is generated at the very tip of the moving body. As the time increases, this whirling structure develops moving upward and detaching from the moving landslide that continues its descent travel.

Furthermore, given that the sloping coast is modeled as a porous media characterized by a low permeability, in which the VARANS equations are solved, it is important to confirm that the flow velocity within the porous media is as small as possible (i.e., nearly zero), that the velocity profiles at the interface surface of the porous media itself are conveniently smooth, and that the mass is conserved throughout the simulation. In the lower panel of Figure 8, the contour plots of the velocity magnitude inside (grayscale colorbar) and outside (red and blue colorbar) the porous media, at the time instant $t = 0.75$ s, are presented. It can clearly be seen that the flow velocity within the porous media exhibits very small values, below 10^{-4} m/s. Furthermore, negligible flow velocity is detectable at the interface surface of the porous media region, testifying that no incoming nor outgoing water flux is observed.

The upper panel of Figure 8 presents the matching behavior of the velocity profiles at the interface surface of the porous media. In this panel the velocity profiles (blue dots) at a given time ($t = 0.75$ s), measured at four virtual gauges ($VG_1, VG_2, VG_3,$ and VG_4 , thin black lines), deployed on the symmetry plane ($y = 1.85$ m) and perpendicularly crossing the porous media surface (i.e., the sloping coast), are represented. Note that the presented values of the profiles do not reflect the real values of the flow velocity magnitudes (shown in the second and third columns of Figure 7 and in the lower panel of Figure 8), as they have been distorted for graphic

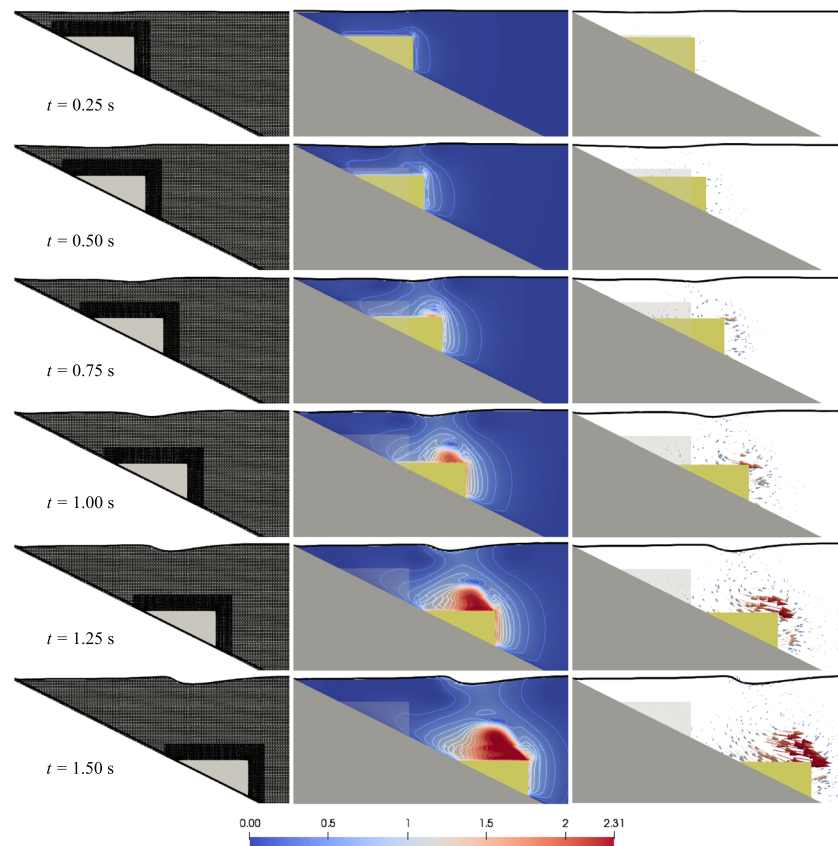


Figure 7. Moving computational grid (first column), contour plot (second column) and vectorial diagram (third column) of the magnitude of the velocity at six selected time instants ($t = 0.25, 0.50, 0.75, 1.00, 1.25,$ and 1.50 s, measured from the beginning of the landslide motion) evaluated along a cross section placed at $y = 1.85$ m. The quantities identified by the colormap are expressed in m/s.

needs to magnify the shape of the profiles themselves. As previously stated, the flow velocity is nearly zero (i.e., blue dots coincide with the thin black lines) within the porous media region, and the flow transition at the porous interface appears to be very smooth. This behavior is clearly detectable looking at VG_1 , VG_3 , and VG_4 but not for VG_2 as the landslide model is passing on the virtual gauge at the considered time step. Thus, at VG_2 the velocity magnitude is zero within the porous media and, consistently, exhibits values different from zero just above the moving body.

Moreover, the mass conservation throughout the entire simulation is discussed. To this end, the mass of both phases (air and water) has been checked during the whole simulation time, resulting in a final variation of $2.46 \cdot 10^{-5}\%$ and $5.42 \cdot 10^{-6}\%$ with respect to the initial fraction of water and air, respectively. To the knowledge of the authors, it is the first time that mass conservation is clearly discussed and in previous studies, where porous media solvers were used (e.g., Higuera et al., 2014a, 2014b; Jacobsen et al., 2015, 2018), the mass was not fully conserved.

To conclude, by using this approach, the CTs can slightly increase as an additional part of the domain (i.e., the porous media) is taken into account. However, this increase is not significant, as the flow velocity is almost zero within the porous region, as shown in the upper left and in the lower panels of Figure 8.

4. Description of the Parametric Simulations

As previously stated, this work aims to investigate the near-field wave characteristics of tsunamis generated by submerged landslides by exploring the effects of different landslide-triggering mechanisms (i.e., change of a_0). Therefore, the new numerical approach has been applied to investigate the tsunami wave features in the near field. Parametric simulations have been performed by varying the initial acceleration a_0 ,

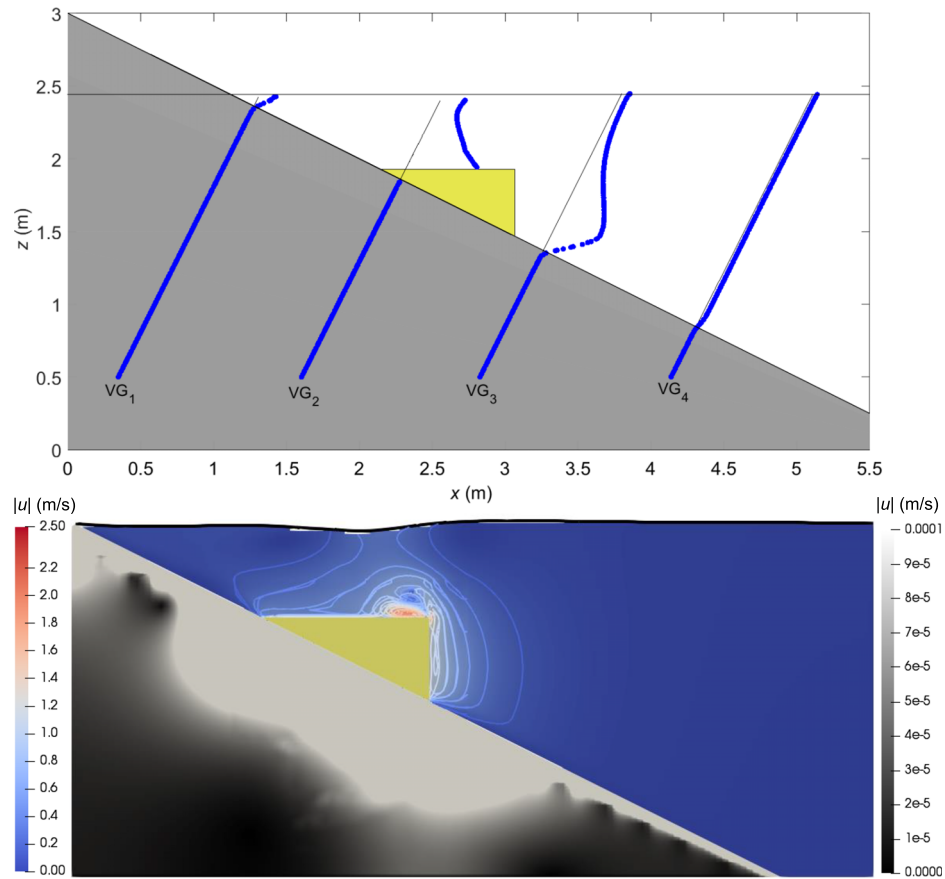


Figure 8. Upper panel: velocity profiles at four virtual gauges deployed on the symmetry plane ($y = 1.85$ m) normal to the porous slope at $t = 0.75$ s. Lower panel: contour plot of the velocity magnitude inside (grayscale colorbar) and outside (red and blue colorbar) the porous media at $t = 0.75$ s.

aiming at investigating different landslide-triggering mechanisms beyond pure gravity driven. Similar experiments have been conducted in the past, although by using completely different approaches and dealing with different layouts, by Watts (1998) and by Romano et al. (2017).

Therefore, three different sets of parametric simulations PSS j (being $j = 1, 2, 3$) have been carried out. For each PSS j nine different values of initial acceleration a_0 (viz., $a_0 = 0.5, 1.0, 1.5, 2.0, 3.0, 4.0, 5.0, 7.0,$ and 8.0 m/s^2) have been used, keeping constant few selected parameters (i.e., landslide dimensions $b, a,$ and $w,$ initial position of the landslide, d/b ratio, and water depth h). Therefore, the nine values of a_0 , accordingly with the other hydrodynamics parameters previously calculated, have been used to obtain, via Equations 11 and 12, the relative landslide motions in terms of $s(t)$ and $u(t)$, respectively. The nine values of initial acceleration have been arbitrarily chosen, by following the precise purpose of extending the range of Hammack number (H_{a_0}), defined as

$$H_{a_0} = \frac{u_t \sqrt{gd}}{a_0 b}, \quad (15)$$

previously explored by experimental studies (e.g., Enet & Grilli, 2007; Romano et al., 2017; Watts, 1998). In particular, to explore those values of H_{a_0} that hardly can be (safely) obtained in laboratory experiments (i.e., $H_{a_0} < 3.0$ and $H_{a_0} > 5.0$).

Hence, a wide range of landslide-triggering mechanisms, dynamics, and rheology (i.e., rock slide, earth slide, debris flow, liquefaction, etc.) is investigated, although a direct link between a_0 and the landslide type is not straightforward to obtain. Indeed, previous studies related to tsunamis generated by submerged landslides (mainly gravity driven) show that a_0 exhibits a wide range of values: for example, a_0 up to 0.06 m/s^2

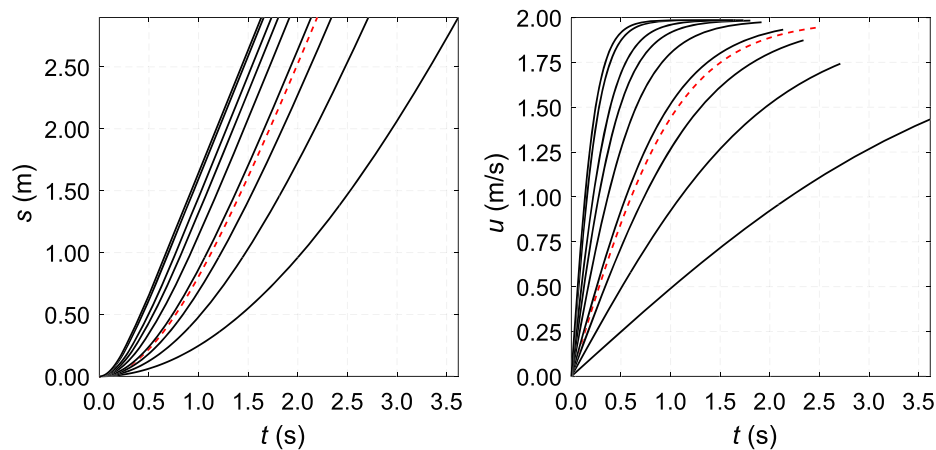


Figure 9. Time series of the landslide displacement (left panel) and of the landslide velocity (right panel) as a function of the initial acceleration a_0 . Red dashed lines refer to the time series of the landslide displacement and velocity related to the experiment of Liu et al. (2005) used for the validation.

(Løvholt et al., 2015), 0.20 m/s^2 (Koh et al., 2016), 0.60 m/s^2 (Janin et al., 2019), 1.20 m/s^2 (Enet & Grilli, 2007), and 1.50 m/s^2 (Sue et al., 2011). Moreover, it is well documented that other phenomena (ground liquefaction, thermal pressurization, etc.) can change the landslide rheology and dynamics resulting in landslides with a higher mobility than that provided by a simple gravity-driven instability. For instance, during the Vajont event it is estimated that an acceleration of 2.60 m/s^2 has been reached due to the thermal pressurization (Veveakis et al., 2007).

In light of the above, the general idea of varying a_0 is to investigate the possible effects, in terms of the generated wave characteristics, of a wide range of landslide-triggering mechanisms. The a_0 values have been chosen arbitrarily, but with the aim of pursuing two main purposes: (a) to investigate the effects of these rapidly evolving landslide phenomena; (b) to enucleate the asymptotic physical features of landslide-generated tsunamis by performing a parametric analysis of a_0 .

The nine landslide motion curves used for each set of parametric simulations are shown in Figure 9 with black lines. The left panel of this figure reports the time series of the landslide displacement, while the right one shows the time series of the landslide velocity. By varying the initial acceleration, the displacement of the landslide, at a given time instant, will change among the nine curves. Therefore, in order to compare similar conditions, the motion of the landslide has been stopped once the body has traveled 2.9 m. This condition is matched at different times depending on a_0 . The red dashed lines refer to the kinematic characteristics of the landslide, namely, time series of displacement (left panel) and velocity (right panel) as from the experiment of Liu et al. (2005). A few parameters have been changed, among different sets, to investigate a wide range of conditions, as shown in Table 2.

5. Analysis of the Near Field: Results and Discussion

This section discusses the near-field wave characteristics. In order to postprocess the numerical results, several virtual wave gauges have been deployed into the domain as shown in the left panel of Figure 10. In this panel the numerical wave gauges (which refer to PSS3) are identified by blue crosses, while the initial shoreline and the initial landslide positions are identified by blue dashed and red continuous lines, respectively. The adopted sensor arrays, partially resembling the sensor layout described in Romano et al. (2013) and later in Bellotti and Romano (2017), consist of concentric circles of wave gauges, having the center in the barycentric position of the landslide (in its initial position).

Therefore, all the free-surface elevation time series from virtual wave gauges have been analyzed to provide a detailed description of the wave features in the near field. The postprocessing analysis is divided as follows:

- Time domain analysis of the free-surface elevation time series;
- Spatial analysis of the wave characteristics;
- Analysis of the synthetic results (i.e., wave crests and troughs) and comparison with previous studies.

Table 2
Names and Parameters of the Parametric Simulations (see Figure 3 for Parameter Identification)

| | PSS1 | PSS2 | PSS3 |
|---------|-------|-------|-------|
| h (m) | 2.44 | 2.55 | 2.52 |
| d (m) | 0.30 | 0.15 | 0.12 |
| d/b | -0.33 | -0.16 | -0.13 |

5.1. Time Domain Analysis of the Free-Surface Elevation Time Series

In this section only the results of five representative virtual wave gauges are represented for each set of simulations, aiming at showing the effects induced by the variation of the initial acceleration on the generated waves. These five wave gauges (G1, G2, G3, G4, and G5) are represented as blue circles in the right panel of the Figure 10.

The results are shown in Figure 11. Each row of this figure reports the results of a simulation set (i.e., PSS1, PSS2, and PSS3), while each column refers to the free-surface elevation time series measured by one of the five wave gauges shown on the right panel of Figure 10 (i.e., the first column refers to the results measured by G1, while the fifth column refers to the ones measured by G5). Each panel contains nine free-surface elevation time series, represented with grayscale (light gray refers to small values of a_0 , while dark gray to large ones).

Figure 11 fully reflects the features of the tsunami generation process. The first column shows that the impulsive phenomenon starts with a free-surface depression, while the second column (i.e., wave gauge placed in the barycentric position of the landslide initial position) shows that a wave crest follows the first large wave trough, as a consequence of the typical rebound of the free surface. The following columns show that the tsunami signal starts with a small wave crest, produced by the landslide piston-like mechanism, followed by a large wave trough and a second wave crest, generally larger than the first one.

Furthermore, Figure 11 highlights the influence of a_0 on the generated wave signals. As far as different values of a_0 are concerned, keeping fixed the other geometrical parameters, the characteristics of the tsunamis change dramatically. The magnitude of the wave characteristics (minimum troughs and maximum crests) increases with a_0 . Additionally, the rising time of the first wave trough decreases, and in general, the wave signals exhibit a narrower and sharper shape (i.e., decreasing wave periods). These preliminary results confirm the experimental findings of Romano et al. (2017), although a different configuration is considered here. A detailed spatial analysis of the wave characteristics is provided in the following sections.

5.2. Spatial Analysis of the Wave Characteristics

A standard time-domain analysis (i.e., wave-by-wave analysis) has been applied to extract the wave characteristics from each free-surface elevation time series measured by the N virtual wave gauges shown on the left panel of Figure 10. The wave characteristics of interest are

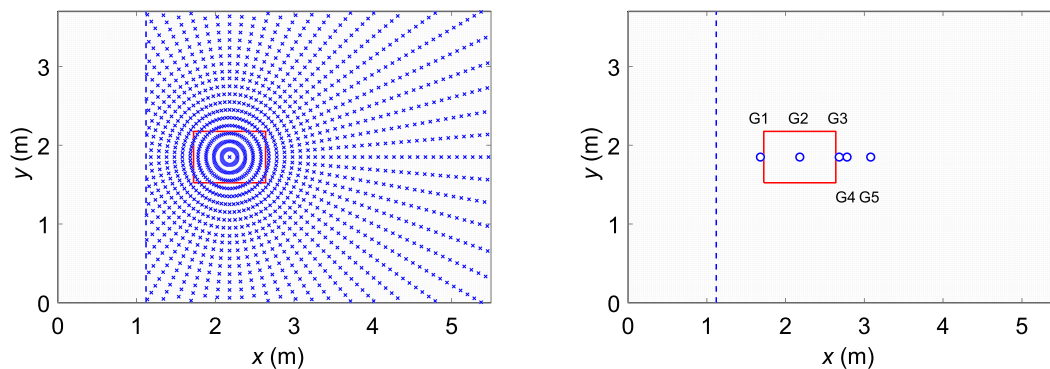


Figure 10. Left panel: plan view of the numerical wave gauges deployed in the domain (blue crosses). Right panel: plan view of the four numerical wave gauges used for the time domain analysis (blue circles). Note that in both panels the initial shoreline position and the initial landslide position are identified by blue dashed and red lines, respectively.

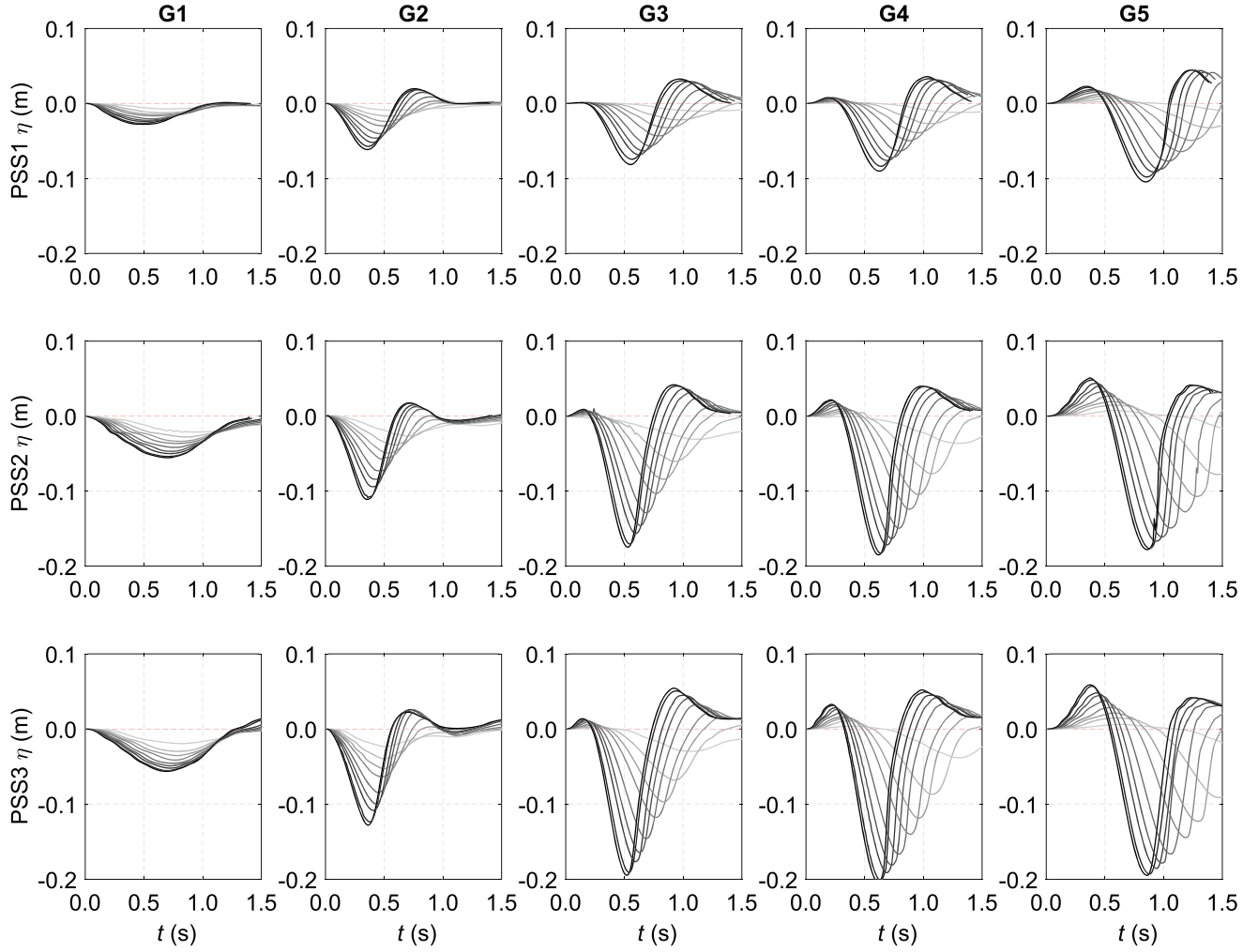


Figure 11. Free-surface elevation time series as a function of the initial acceleration a_0 . Note that the rows of the figure (from up to down) refer to PSS1, PSS2, and PSS3, respectively, while the columns of the figure (from left to right) refer to the measurements of the virtual wave gauges reported in the right panel of Figure 10 (from left to right). Each panel contains nine curves referring to $a_0 = 0.5, 1.0, 1.5, 2.0, 3.0, 4.0, 5.0, 7.0, 8.0 \text{ m/s}^2$; light gray refers to small values of a_0 , while dark gray to large ones.

- $\eta_c^{\max-i}$: maximum wave crest detected in the i^{th} ($i = 1, 2, \dots, N$) time series (i.e., spatial envelope of the maximum wave crests).
- $\eta_t^{\min-i}$: minimum wave trough detected in the i^{th} ($i = 1, 2, \dots, N$) time series (i.e., spatial envelope of the minimum wave troughs).
- η_c^{\max} : maximum wave crest (i.e., maximum value among the $\eta_c^{\max-i}$).
- η_t^{\min} : minimum wave trough (i.e., minimum value among the $\eta_t^{\min-i}$).
- η_{\max} : absolute value of the maximum free-surface oscillation detected at the N virtual wave gauges, defined as $\eta_{\max} = \max(|\eta_c^{\max}|, |\eta_t^{\min}|)$.
- $T_{\eta_{\max}}$: wave period related to the wave containing η_{\max} .
- c_t^{1st} : mean wave celerity of the first wave trough (measured along the landslide path).
- η_0 : absolute value of the maximum free-surface oscillation measured at the wave gauges having coordinates (x_0, y_0) , that is, the barycentric position of the landslide at its initial position, defined as $\eta_0 = \max(|\eta(x_0, y_0, t)|)$.

Figure 12 shows an example of the spatial analysis. This figure, referring to the results of PSS3 ($a_0 = 2.0 \text{ m/s}^2$), represents the spatial layout of $\eta_c^{\max-i}$ (left panel) and $\eta_t^{\min-i}$ (right panel). In both panels the initial

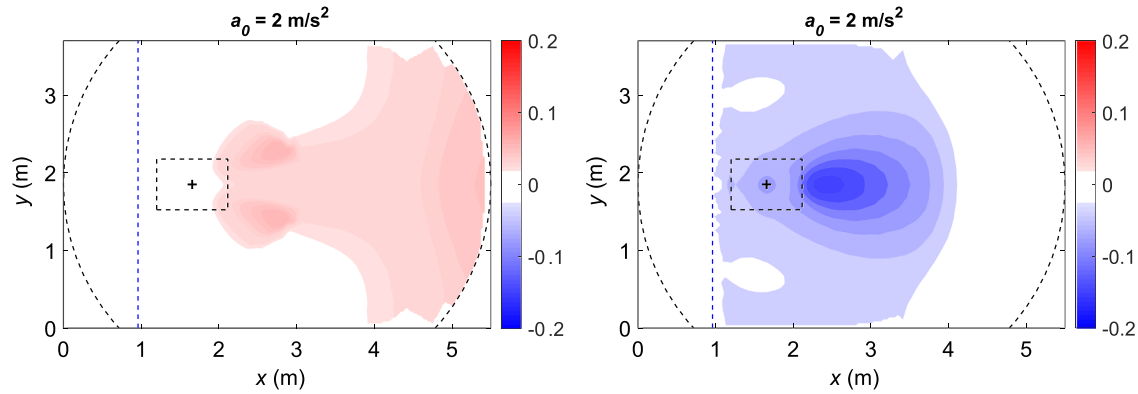


Figure 12. Spatial layout of $\eta_c^{\max-i}$ (left panel) and $\eta_t^{\min-i}$ (right panel) obtained from one simulation of PSS3 ($a_0 = 2.0 \text{ m/s}^2$). In each panel the initial shoreline, the initial landslide, and the initial landslide's barycentric positions are identified by blue dashed lines, black dashed lines, and black crosses, respectively.

shoreline and the initial position of the landslide are identified by blue and black dashed lines, respectively. It is worth noticing that $\eta_c^{\max-i}$ and $\eta_t^{\min-i}$ do not necessarily occur simultaneously. Moreover, Figure 12 shows that the numerical results exhibit a very good spatial symmetry around the symmetry plane at $y_0 = 1.85 \text{ m}$, even considering that the represented quantities are not synchronous. Additionally, both panels emphasize the lack of transversal modes; this is expected as the numerical wave tank is not narrow, especially if compared with the landslide width. Therefore, to simplify the comparison of the wave characteristics in the same plot, as well as to minimize the number of figures, the spatial representation of $\eta_c^{\max-i}$ and $\eta_t^{\min-i}$ has been performed by splitting each contour plot into two parts as follows: above the symmetry plane the spatial layout of $\eta_c^{\max-i}$ is represented, while below the symmetry plane the spatial layout of $\eta_t^{\min-i}$ is plotted.

Figures 13, 14, and 15 show the results of the spatial analysis of $\eta_c^{\max-i}$ and $\eta_t^{\min-i}$ as obtained for the parametric simulations PSS1, PSS2, and PSS3, respectively. To allow the comparison of the wave characteristics between different simulations and different sets of simulations, a single color bar, spanning between -0.20 m and $+0.20 \text{ m}$, has been used for all plots.

The nine panels of Figure 13 clearly show that PSS1 exhibits the smallest wave characteristics of the three considered sets. The large d/b ratio ($d/b = -0.33$), together with the small values of the landslide initial accelerations a_0 (first row of the figure), results in small tsunamis, typically characterized by significantly larger troughs than crests. Nevertheless, as the initial acceleration increases (second and third rows of the figure), the generated tsunamis, and accordingly the wave characteristics, increase as well. Minimum wave troughs are always larger (up to two times) than the maximum wave crests, as expected from submerged landslide tsunamis. Furthermore, from the fifth initial acceleration ($a_0 = 3.0 \text{ m/s}^2$), the minimum wave trough starts to have significant values shoreward from the initial landslide position, that is, close to the shoreline. Finally, it can be seen that from the sixth initial acceleration ($a_0 = 4.0 \text{ m/s}^2$), some reflection phenomena, between the wave trough and the numerical wave tank walls, occur. These phenomena, detected throughout all the simulation sets for increasing a_0 , are within the time window used for the presented analysis, limited to the portion of domain adjacent to the tank walls and do not contaminate the near-field wave characteristics.

Similar considerations arise from Figures 14 and 15 for PSS2 and PSS3, respectively. In these cases, the contour plots show that larger tsunamis, if compared with those of PSS1, characterize these two sets. This is expected, as d/b is smaller than that of PSS1 ($d/b = -0.16$ for PSS2 and $d/b = -0.13$ for PSS3). The first initial acceleration $a_0 = 0.5 \text{ m/s}^2$ produces small tsunamis. Starting from the second value of a_0 the tsunami crests and troughs exhibit larger values throughout the domain. No significant differences can be detected among the two simulation sets. Furthermore, the figures show some wave reflection, between the wave trough and the numerical wave tank walls, without contaminating the near-field wave features. The spatial analysis of the parametric simulations, shown in Figures 13, 14, and 15, confirms that the influence of the initial acceleration a_0 on the tsunami generation mechanisms and on the near-field wave features is significant.

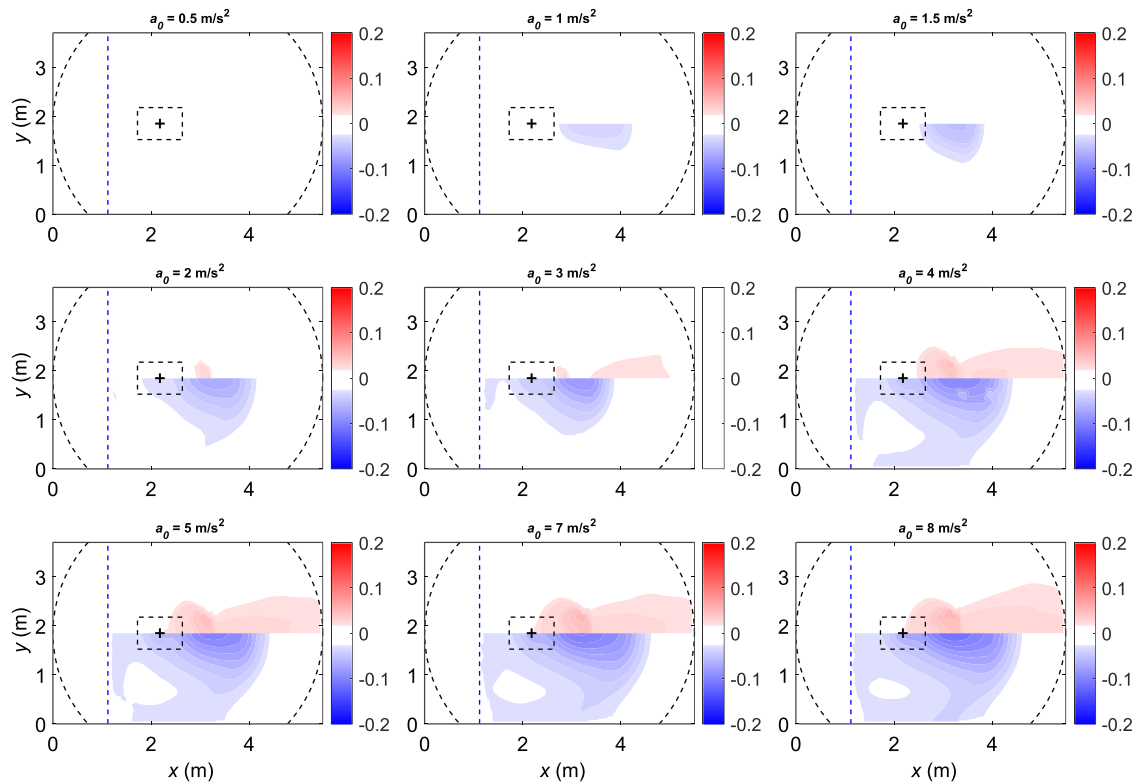


Figure 13. Spatial layout of $\eta_c^{\max-i}$ (upper part of each panel) and $\eta_c^{\min-i}$ (lower part of each panel) obtained from the nine parametric simulations of PSS1. In each panel the initial shoreline, the initial landslide, and the initial landslide's barycentric positions are identified by blue dashed lines, black dashed lines, and black crosses, respectively.

Figure 16 is made of two panels representing the following quantities as a function of a_0 : η_c^{\max} and η_i^{\min} (square and diamond markers, respectively) in the left panel; η_{\max} (circle markers) in the right panel. Note that in the figure red markers refer to the results of PSS1, while blue and black markers refer to the ones of PSS2 and PSS3, respectively. As a_0 increases, η_c^{\max} increases and η_i^{\min} decreases. This rate of increase (and decrease) appears to be less than linear for all the considered sets. Furthermore, as previously argued, the minima wave troughs are always larger (in modulus) than the maxima wave crests, up to two times. Both η_c^{\max} and η_i^{\min} seem to approach an asymptotic value for $a_0 > 4.0 \text{ m/s}^2$. This behavior suggests that, for fixed sets of governing parameters, even by increasing a_0 the maxima wave crests (and minima wave troughs) are not further increasing (or decreasing). A saturation effect on the tsunami generation mechanism is observed. This effect is confirmed by previous studies. Indeed, Tinti and Bortolucci (2000) pointed out a similar behavior by introducing the Froude number of the landslide to quantify the saturation. Nevertheless, they have evaluated mainly the landslide velocity and the duration of the movement, while here with a_0 a different descriptor of the landslide kinematics has been investigated. In addition, similar saturation has also been observed experimentally for edge waves, induced by subaerial landslides (Di Risio, De Girolamo, et al., 2009; Heller & Spinnenken, 2015), which are known to play a crucial role in the tsunami alongshore propagation and interaction with the coast (Romano et al., 2013).

In the right panel of Figure 16 η_{\max} is plotted as a function of a_0 , where red markers refer to PSS1, while blue and black markers refer to PSS2 and PSS3, respectively. Consistently to what was discussed for η_c^{\max} and η_i^{\min} , the smallest values of η_{\max} refer to PSS1, while larger values characterize PSS2 and PSS3. The behavior of η_{\max} , as a function of a_0 , clearly resembles the one observed in the left panel of Figure 16. As a_0 increases, η_{\max} increases as well, with a rate of increase less than linear for all the considered sets, approaching to asymptotic values. Thus, the saturation effect is noticeable also for η_{\max} . Indeed, also this important parameter exhibits a decrease of the growth rate for increasing values of a_0 . Moreover, η_{\max} never occurs in

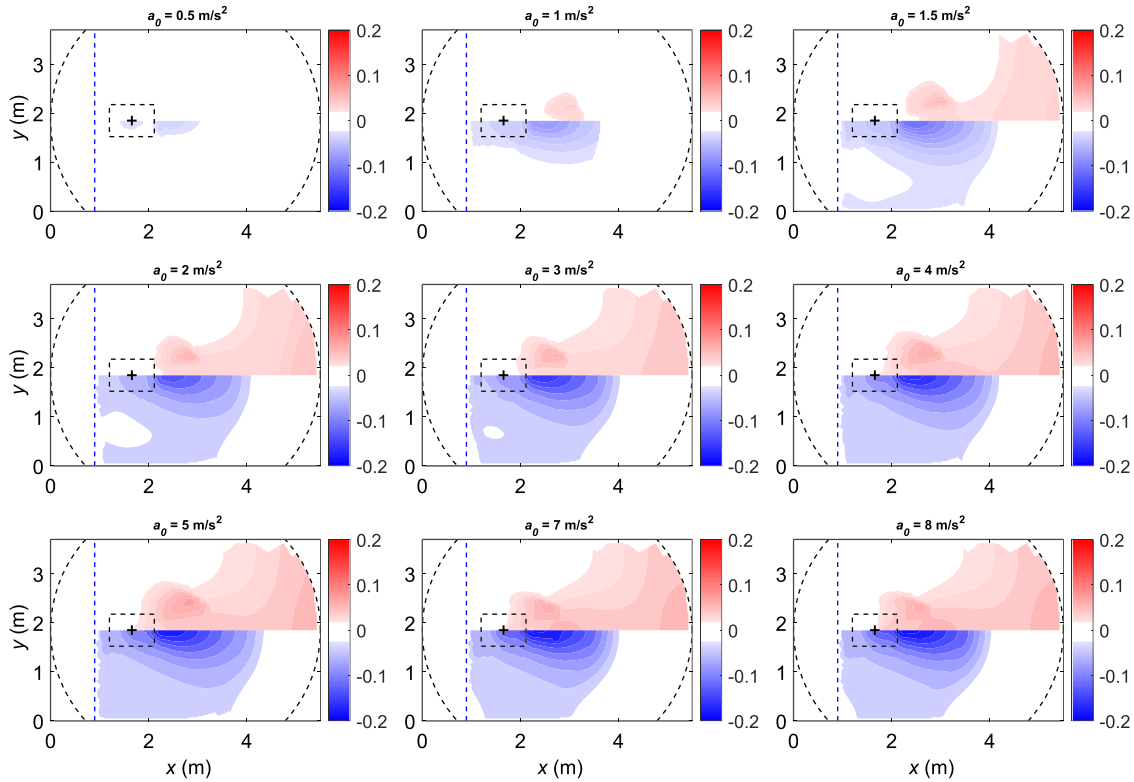


Figure 14. Spatial layout of $\eta_c^{\max-i}$ (upper part of each panel) and $\eta_c^{\min-i}$ (lower part of each panel) obtained from the nine parametric simulations of PSS2. In each panel the initial shoreline, the initial landslide, and the initial landslide's barycentric positions are identified by blue dashed lines, black dashed lines, and black crosses, respectively.

correspondence of the barycentric coordinates of the landslide evaluated at the initial position, which can also be seen in Figures 13, 14, and 15.

The left panel of Figure 17 represents the wave period $T_{\eta_{\max}}$ as a function of a_0 with the common notation. As previously outlined, $T_{\eta_{\max}}$ has been obtained by carrying out a zero-crossing analysis on the apparent wave (i.e., the portion of the free-surface elevation time series) that contains η_{\max} . The left panel of Figure 17 shows that $T_{\eta_{\max}}$ decreases as a_0 increases. This aspect confirms what has been proposed based on Figure 11. The wave periods exhibit an average value of about 2.0 s for the smallest a_0 , while for increasing a_0 , the values of $T_{\eta_{\max}}$ decrease less than linearly, reaching on average an asymptotic value of about 1.0 s. Therefore, a saturation mechanism can also be noticed for $T_{\eta_{\max}}$, confirming that, for increasing a_0 , no more energy can be effectively transferred to the water to generate larger waves. Finally, small differences in $T_{\eta_{\max}}$ are detected among the three sets of simulations, among which only d/b changes. Nevertheless, it should be noticed that the largest wave periods pertain to PSS1.

The right panel of Figure 17 shows the mean celerity of the first wave trough c_t^{1st} with the common notation and the mean velocity of the landslide body u_l (red triangles) as a function of the initial acceleration a_0 . Note that the mean celerities of the first wave trough have been calculated by using the free-surface elevation time series measured by those wave gauges placed parallel to the landslide path, starting from the barycentric position of the landslide. This panel shows that also the mean celerities of the first wave trough saturate, similar to the wave periods and wave crests/troughs. For the smaller values of a_0 , c_t^{1st} is in the order of 0.8 m/s (for all the tested configurations). As a_0 increases, the mean celerities of the first wave trough increase less than linearly, reaching a maximum value of about 1.6 m/s. Negligible differences in c_t^{1st} can be detected among the three sets of simulations. c_t^{1st} for the four smaller values of a_0 is on average identical to u_l . Starting from the fifth value of a_0 these two parameters start to diverge, as u_l is always larger than c_t^{1st} . In other words, u_l starts to be larger than c_t^{1st} approximately as the saturation region begins.

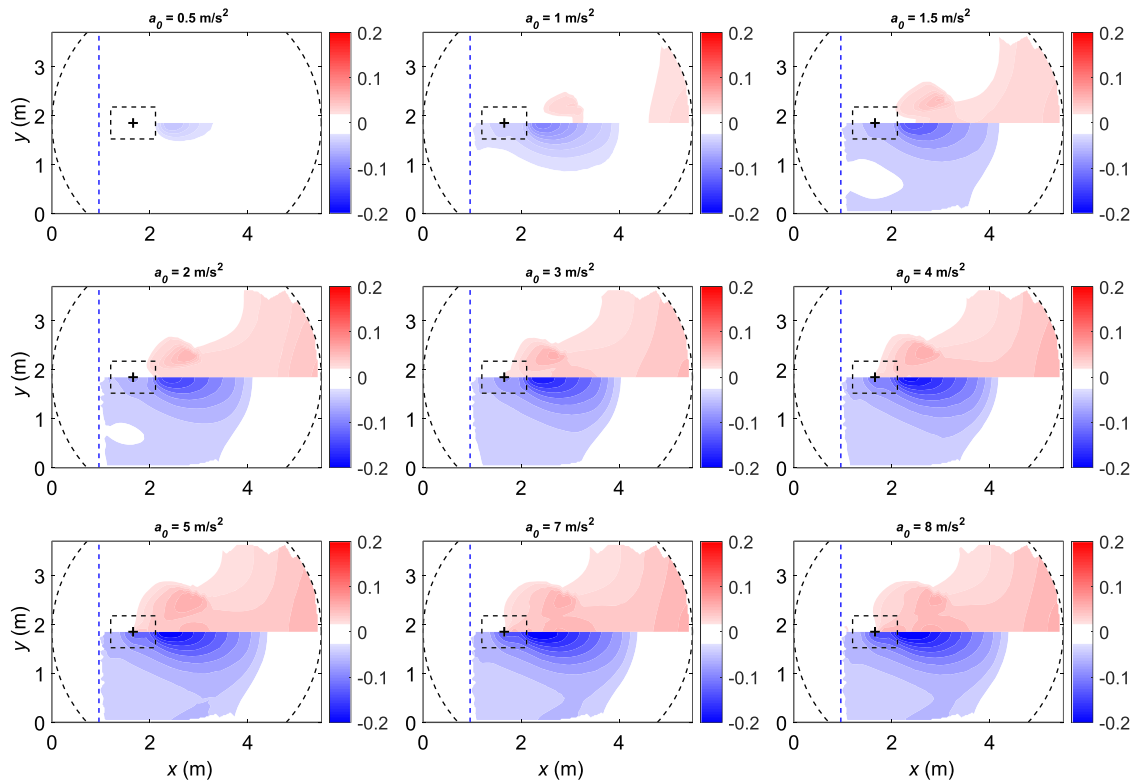


Figure 15. Spatial layout of $\eta_c^{\max-i}$ (upper part of each panel) and $\eta_c^{\min-i}$ (lower part of each panel) obtained from the nine parametric simulations of PSS3. In each panel the initial shoreline, the initial landslide, and the initial landslide's barycentric positions are identified by blue dashed lines, black dashed lines, and black crosses, respectively.

Another parameter of interest, widely used in the scientific literature (e.g., Enet & Grilli, 2007; Romano et al., 2017; Watts, 1998) to describe the wave features of the tsunamis generated by submerged landslides, is η_0 . This parameter is crucial to describe the tsunami wave properties in the near field as it represents the maximum free-surface oscillation measured at the barycentric position of the landslide. In Figure 18 the values of η_0 , related to each set of parametric simulations, are reported as a function of a_0 (circle markers). The

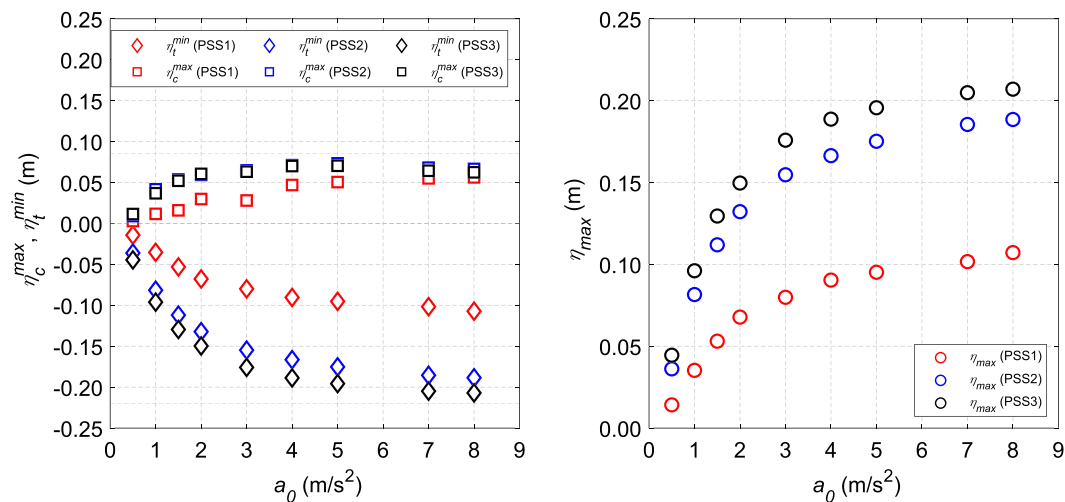


Figure 16. Left panel: η_c^{\max} (square markers) and η_c^{\min} (diamond markers) as a function of the initial acceleration a_0 . Right panel: η_{\max} (circle markers) as a function of the initial acceleration a_0 .

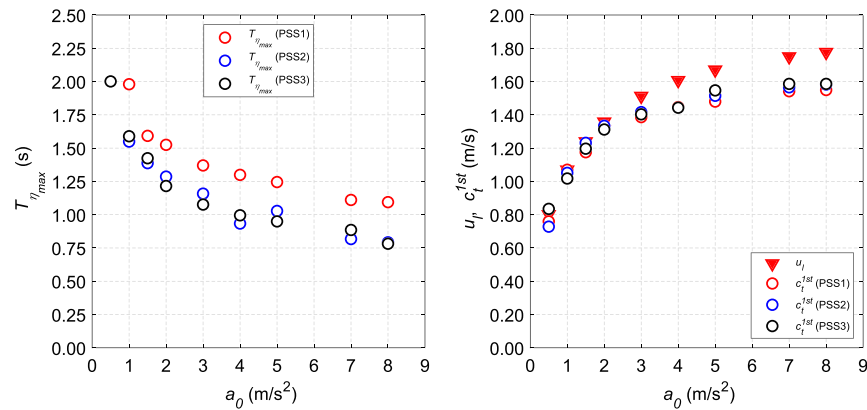


Figure 17. Left panel: wave period $T_{\eta_{max}}$ as a function of the initial acceleration a_0 . Right panel: mean celerity of the first wave trough c_t^{1st} (circle empty markers) and mean velocity of the landslide body u_l (red triangles) as a function of the initial acceleration a_0 .

smallest values of η_0 are observed for PSS1, while as PSS2 and PSS3 are considered, similar values of η_0 occur. Figure 18, in analogy to Figure 16 for η_c^{max} and η_t^{min} , and Figure 17 for $T_{\eta_{max}}$ and c_t^{1st} , confirms the general behavior of the wave characteristics described so far. Indeed, Figure 18 shows that η_0 , for all the investigated simulation sets, increases as a_0 increases, exhibiting a less than linear growth that approaches asymptotic values for increasing values of a_0 (i.e., saturation), resembling the behavior of η_{max} (right panel of Figure 16). The spatial analysis shown so far confirms and extends the findings of previous works on tsunamis generated by submarine landslides (Enet & Grilli, 2007; Romano et al., 2017; Tinti & Bortolucci, 2000; Watts, 1998). Therefore, in order to further improve the understanding of the effect of a_0 on the tsunami wave properties in the near field, a comparison between present results and results from previous studies is presented in the following section.

5.3. Analysis of the Synthetic Results

In this section the analysis of the synthetic results is presented. The wave characteristics, obtained from the numerical results and discussed in the previous section, have been analyzed and presented in the form of a

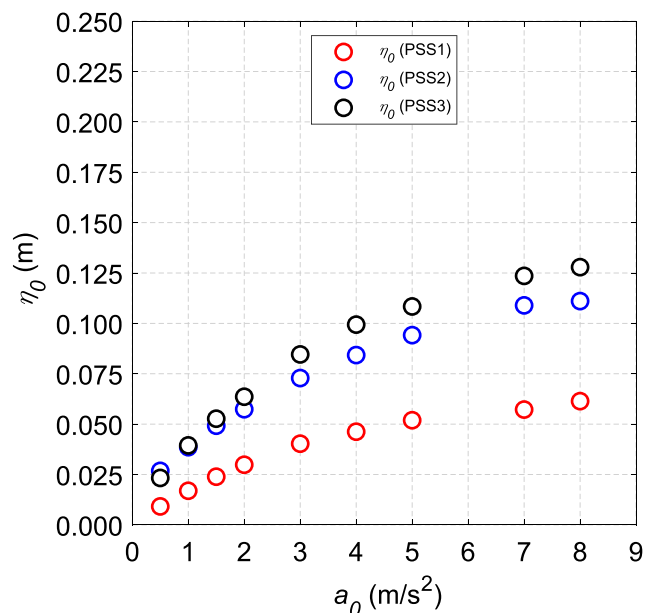


Figure 18. η_0 as a function of the initial acceleration a_0 .

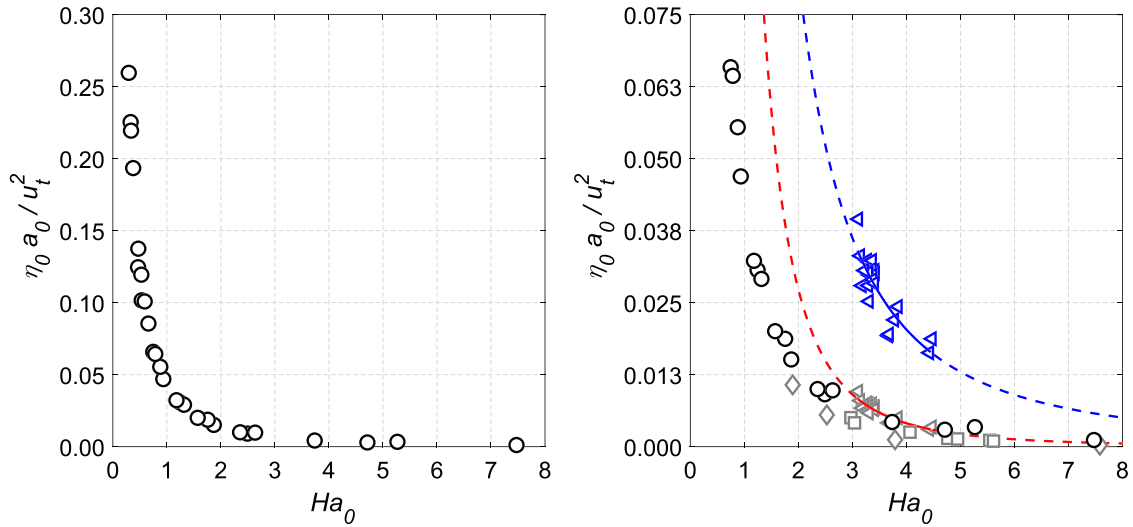


Figure 19. Dimensionless wavemaker plot, as a function of the Hammack number H_{a_0} , obtained by the numerical simulations (left panel). Zoom of the dimensionless wavemaker plot by using several sources of data: new numerical parametric simulations, empty black circles; 2-D- and 3-D-corrected experimental data of Watts (1998), empty blue and gray triangles respectively; 2-D- and 3-D-corrected best fitting curves obtained by Watts (1998), blue and red lines, respectively; experimental data of Enet and Grilli (2007), empty gray squares; 3-D experimental data of Romano et al. (2017), empty gray diamonds (right panel). Note that dashed lines refer to the fitting curves evaluated outside the experimental range.

so-called “nondimensional wavemaker curve,” as carried out by Watts (1998) for 2-D experimental data obtained for a wedge-shaped body sliding on a 45° incline (see Figure 6 of Watts, 1998). The wavemaker curve has been created by representing the maximum nondimensional wave amplitude $\eta_0 a_0 / u_t^2$ as a function of the Hammack number H_{a_0} .

The dimensionless wave amplitudes, calculated from the numerical simulation results, are reported in the left panel of Figure 19 with empty black circles. The range $0.3 \leq H_{a_0} \leq 7.5$ has been investigated. The arrangement of the numerical data exhibits a power law decay that closely resembles the behavior identified by Watts (1998) on the basis of laboratory tests. Further experimental data have been analyzed in this form and reported on the right panel of Figure 19. Firstly, the 2-D experimental results obtained by Watts (1998) are plotted as empty blue triangles, together with the fitting curve represented as a continuous blue line, within the experimental range $3.0 \leq H_{a_0} \leq 4.5$, and as a dashed blue line, outside the experimental range. It can be seen that the present numerical results lie at a different position with respect to those by Watts (1998), although the general arrangement of the two data sets is very similar. The data obtained by Watts (1998) are 2-D. Therefore, in order to directly compare the 2-D data set with the 3-D one, a correction formula has been applied to the 2-D data and to the relative fitting curve. The correction formula, provided by Watts et al. (2005), reads as follows:

$$\eta_{0,3D} = \eta_{0,2D} \left(\frac{w}{w + \lambda_0} \right), \quad (16)$$

where w is the landslide width and $\lambda_0 = u_t \sqrt{gd}/a_0$, although it is worth noticing that Heller and Spinneken (2015) pointed out that Equation 16 may give rise to small conversion factors, at least if subaerial slides are considered. The corrected data are presented in the right panel of Figure 19 as empty gray triangles, while the fitting curve is shown in the same plot as a continuous red line, within the experimental range of H_{a_0} , and as a dashed red line, outside the experimental range. Within the Hammack number range investigated by Watts (1998), the numerical and experimental data are in a very good agreement ($RMSE = 0.5 \cdot 10^{-4}$), while outside the considered range the numerical results slightly deviate from the fitting curve for $H_{a_0} < 3.0$ and still remain in good agreement with the fitting curve for $H_{a_0} > 4.5$.

The data described so far (both numerical and experimental), and presented on the right panel of Figure 19, refer to similar geometries of the problem, that is, wedge-shaped landslides sliding on plane slopes, although

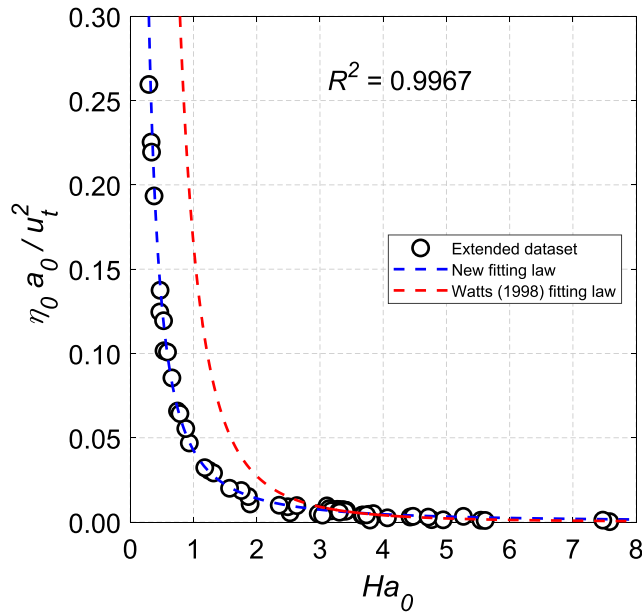


Figure 20. Dimensionless wavemaker curve, as a function of the Hammack number H_{a_0} , with the extended data set, based on different experimental and numerical results (empty black circles). The new (present work) and the previous (Watts, 1998) best fitting curves are represented by blue and red dashed lines, respectively.

having different inclination angles, namely, 45° (Watts, 1998) and 26.56° (present study). It is interesting to extend the current representation to completely different geometries and landslide shapes. The two 3-D data sets from Enet and Grilli (2007) and Romano et al. (2017) are therefore introduced. Specifically, the experiments carried out by Enet and Grilli (2007) refer to a smooth Gaussian-shaped landslide body sliding on a 15° inclined plane slope, while the experiments carried out by Romano et al. (2017) refer to a semi-ellipsoidal-shaped landslide body sliding along a 18° inclined flank of a conical island. These data have been added on the right panel of Figure 19 as empty gray squares (Enet & Grilli, 2007) and empty gray diamonds (Romano et al., 2017), respectively.

These additional data are in good agreement with the previously discussed ones, exhibiting the characteristic power law decay. The Hammack number experimental range, related to these extra sources of data, spans in the interval $1.9 \leq H_{a_0} \leq 7.5$, thus wider than that explored by Watts (1998) but narrower than that investigated in the present study. Therefore, the considered sources of data, obtained by using different techniques, geometries, and configurations, form an extended data set spanning a wider range of H_{a_0} (i.e., $0.3 \leq H_{a_0} \leq 7.5$). Moreover, looking at the right panel of Figure 19, it can be seen that the fitting law proposed by Watts (1998) is obviously not adequate to predict the nondimensional wave amplitude out of the tested experimental range, in particular if small values of the Hammack number (i.e., $H_{a_0} < 3.0$) are considered.

In light of the above, this extended data set has been used to obtain a new fitting function in the form of a power law, following the approach by Watts (1998), as follows:

$$\frac{\eta_0 a_0}{u_t^2} = \tilde{\alpha} H_{a_0}^{-\tilde{\beta}}, \quad (17)$$

where $\tilde{\alpha} = 0.04263$ and $\tilde{\beta} = -1.596$. The proposed fitting curve, together with the extended database, is presented in Figure 20 with the blue dashed line and black empty circles, respectively. Figure 20 shows that the proposed fitting law is able to describe the arrangement of the fitted data with an excellent accuracy. This is also confirmed by the large coefficient of determination ($R^2 = 0.9967$). Indeed, all the points that form the database exhibit a very small scatter from the new fitting line. Furthermore, in the same plot, the fitting law proposed by Watts (1998) is represented with a red dashed line. The nondimensional wavemaker curve obtained by Watts (1998) appears to be very accurate in describing the experimental and numerical results for $H_{a_0} \geq 3.0$, even for values of the Hammack number larger than that explored by Watts (1998). While for smaller values of H_{a_0} the fitting law obtained by Watts (1998) is not able to accurately predict the nondimensional tsunami wave amplitude. On the contrary, the proposed fitting curve obtained with an extended database is more effective in predicting the nondimensional wave amplitude in the near field, especially for large initial accelerations ($H_{a_0} < 3.0$).

6. Concluding Remarks and Ongoing Research

In this paper a detailed numerical analysis of the near-field wave characteristics of tsunamis generated by submerged landslides has been presented. A new method for numerically modeling tsunamis generated by rigid and impermeable submerged landslides with OpenFOAM® has been presented and validated. The proposed method consists in coupling the overset mesh technique, which is a new and promising method in the coastal engineering field, with the well-known porous media approach currently implemented in IHFOAM. This coupling allows to overcome a restriction of the overset mesh method that does not allow the modeling of a rigid body moving in touch with an impermeable surface. The excellent agreement between the numerical results and the experimental data of Liu et al. (2005) highlights the ability of the proposed approach in reproducing such a complex phenomenon.

The numerical method, validated against experimental data, has been applied to perform an extensive set of new parametric simulations aimed at exploring the influence of the landslide-triggering mechanisms on the generated wave characteristics. The same configuration as for the validation has been used. Three sets of parametric simulations, each one characterized by a different value of d/b (i.e., the ratio of the vertical distance between the still water level and the landslide's upper face d to the length of the landslide b , $d/b = -0.33, -0.16, -0.13$), have been carried out by varying the initial acceleration a_0 , in order to explore different landslide-triggering mechanisms. The numerical results allowed to perform a quantitative and detailed analysis of the tsunami properties in the near field. The new numerical results, which are in good agreement with previous experimental studies (e.g., Romano et al., 2017), have shown that, in general, the wave characteristics in the near field vary as a function of a_0 . In particular, for increasing values of a_0 , the wave crests and troughs tend to increase, the wave periods tend to decrease, and the mean celerities of the first wave troughs tend to increase. All the mentioned quantities suffer a saturation mechanism for increasing values of a_0 (i.e., no more energy can be effectively transferred from landslide to water to generate larger waves), confirming the findings of Tinti and Bortolucci (2000).

Furthermore, the numerical data have been represented, together with previous experimental ones obtained for different geometries and configurations, in the form of a “nondimensional wavemaker curve,” as proposed by Watts (1998). The very good agreement among these different sources of data, together with the extended data set provided by the new numerical simulations that consider a wider range of the governing parameters (i.e., $0.3 \leq H_{a_0} \leq 7.5$), allowed to obtain a new fitting curve for predicting the wave characteristics in the near field, induced by rigid and impermeable submerged landslides, as a function of the Hammack number H_{a_0} . In the present work only tsunamis generated by rigid and impermeable submerged landslides have been considered. Although this represents an approximation of the real submerged landslide behavior, it is well demonstrated in the scientific literature (Grilli et al., 2009) that the landslide deformation does not play a significant role on submarine landslide tsunami features in the slide early time kinematics, which at short time scales is mainly governed by the initial acceleration. Nevertheless, as far as ongoing research is concerned, the effects of the landslide deformation and porosity have to be introduced and modeled, especially if subaerial landslides are considered.

Acknowledgments

The data presented in this research are provided as supplements (i.e., supporting information, SI).

References

- Abadie, S., Harris, J., Grilli, S., & Fabre, R. (2012). Numerical modeling of tsunami waves generated by the flank collapse of the Cumbre Vieja Volcano (La Palma, Canary Islands): Tsunami source and near field effects. *Journal of Geophysical Research*, *117*, C05030. <https://doi.org/10.1029/2011JC007646>
- Abadie, S., Morichon, D., Grilli, S., & Glockner, S. (2010). Numerical simulation of waves generated by landslides using a multiple-fluid Navier-Stokes model. *Coastal Engineering*, *57*(9), 779–794.
- Bellotti, G., Cecioni, C., & De Girolamo, P. (2008). Simulation of small-amplitude frequency-dispersive transient waves by means of the mild-slope equation. *Coastal Engineering*, *55*(6), 447–458.
- Bellotti, G., Di Risio, M., & De Girolamo, P. (2009). Feasibility of tsunami early warning systems for small volcanic islands. *Natural Hazards and Earth System Sciences*, *9*(6), 1911–1919.
- Bellotti, G., & Romano, A. (2017). Wavenumber-frequency analysis of landslide-generated tsunamis at a conical island. Part II: EOF and modal analysis. *Coastal Engineering*, *128*, 84–91.
- Brackbill, J. U., Kothe, D. B., & Zemach, C. (1992). A continuum method for modeling surface tension. *Journal of Computational Physics*, *100*(2), 335–354.
- Bullard, G., Mulligan, R., Carreira, A., & Take, W. (2019). Experimental analysis of tsunamis generated by the impact of landslides with high mobility. *Coastal Engineering*, *152*, 103538.
- Cecioni, C., Romano, A., Bellotti, G., Di Risio, M., & De Girolamo, P. (2011). Real-time inversion of tsunamis generated by landslides. *Natural Hazards & Earth System Sciences*, *11*(9), 2511–2520.
- Chen, F., Heller, V., & Briganti, R. (2019). Numerical simulation of tsunamis generated by iceberg calving. In *Proc. 38th IAHR World Congress* (pp. 5640–5649).
- Chen, H., Qian, L., Ma, Z., Bai, W., Li, Y., Causon, D., & Mingham, C. (2019). Application of an overset mesh based numerical wave tank for modelling realistic free-surface hydrodynamic problems. *Ocean Engineering*, *176*, 97–117.
- Clous, L., & Abadie, S. (2019). Simulation of energy transfers in waves generated by granular slides. *Landslides*, *17*, 1663–1679.
- del Jesus, M., Lara, J. L., & Losada, I. J. (2012). Three-dimensional interaction of waves and porous coastal structures: Part I: Numerical model formulation. *Coastal Engineering*, *64*, 57–72.
- Devolder, B., Rauwoens, P., & Troch, P. (2017). Application of a buoyancy-modified $k-\omega$ SST turbulence model to simulate wave run-up around a monopile subjected to regular waves using OpenFOAM®. *Coastal Engineering*, *125*, 81–94.
- Di Paolo, B., Lara, J. L., Barajas, G., Paci, A., & Losada, I. J. (2018). Numerical analysis of wave and current interaction with moored oating bodies using overset method. In *Asme 2018 37th International Conference on Ocean, Offshore and Arctic Engineering* (pp. V002T08A037-V002T08A037).
- Di Risio, M., Bellotti, G., Panizzo, A., & De Girolamo, P. (2009). Three-dimensional experiments on landslide generated waves at a sloping coast. *Coastal Engineering*, *56*(5-6), 659–671. <https://doi.org/10.1016/j.coastaleng.2009.01.009>

- Di Risio, M., De Girolamo, P., Bellotti, G., Panizzo, A., Aristodemo, F., Molfetta, M. G., & Petrillo, A. F. (2009). Landslide-generated tsunamis runup at the coast of a conical island: New physical model experiments. *Journal of Geophysical Research*, *114*, C01009. <https://doi.org/10.1029/2008JC004858>
- Eneš, F., & Grilli, S. T. (2007). Experimental study of tsunami generation by three-dimensional rigid underwater landslides. *Journal of Waterway Port Coastal and Ocean Engineering-ASCE*, *133*(6), 442–454. [https://doi.org/10.1061/\(ASCE\)0733-950X\(2007\)133:6\(442\)](https://doi.org/10.1061/(ASCE)0733-950X(2007)133:6(442))
- Engelund, F. (1953). On the laminar and turbulent flows of ground water through homogeneous sand. *Transactions of the Danish Academy of Technical Sciences*, *3*, 356–361.
- Fritz, H. M., Hager, W. H., & Minor, H. E. (2004). Near field characteristics of landslide generated impulse waves. *Journal of Waterway, Port, Coastal, and Ocean Engineering*, *130*(6), 287–302.
- Fritz, H. M., Hillaire, J. V., Molière, E., Wei, Y., & Mohammed, F. (2012). Twin tsunamis triggered by the 12 January 2010 Haiti earthquake. *Pure and Applied Geophysics*, *170*, 1463–1474.
- Fritz, H. M., Mohammed, F., & Yoo, J. (2009). Lituya Bay landslide impact generated mega-tsunami 50th anniversary. *Pure and Applied Geophysics*, *166*(1-2), 153–175.
- Grilli, S. T., Shelby, M., Kimmoun, O., Dupont, G., Nicolsky, D., Ma, G., et al. (2017). Modeling coastal tsunami hazard from submarine mass failures: Effect of slide rheology, experimental validation, and case studies off the US East Coast. *Natural Hazards*, *86*(1), 353–391.
- Grilli, S. T., Tappin, D. R., Carey, S., Watt, S. F., Ward, S. N., Grilli, A. R., et al. (2019). Modelling of the tsunami from the December 22, 2018 lateral collapse of Anak Krakatau volcano in the Sunda Straits, Indonesia. *Scientific Reports*, *9*, 11,946.
- Grilli, S. T., Taylor, O. D. S., Baxter, C. D., & Marezki, S. (2009). A probabilistic approach for determining submarine landslide tsunami hazard along the upper east coast of the United States. *Marine Geology*, *264*(1-2), 74–97.
- Grilli, S. T., & Watts, P. (2005). Tsunami generation by submarine mass failure. I: Modeling, experimental validation, and sensitivity analyses. *Journal of Waterway, Port, Coastal, and Ocean Engineering*, *131*(6), 283–297.
- Heidarzadeh, M., Ishibe, T., Sandanbata, O., Muhari, A., & Wijanarto, A. B. (2020). Numerical modeling of the subaerial landslide source of the 22 December 2018 Anak Krakatoa volcanic tsunami, Indonesia. *Ocean Engineering*, *195*, 106733. <https://doi.org/10.1016/j.oceaneng.2019.106733>
- Heller, V., Bruggemann, M., Spinneken, J., & Rogers, B. D. (2016). Composite modelling of subaerial landslide–tsunamis in different water body geometries and novel insight into slide and wave kinematics. *Coastal Engineering*, *109*, 20–41.
- Heller, V., & Hager, W. H. (2010). Impulse product parameter in landslide generated impulse waves. *Journal of Waterway, Port, Coastal, and Ocean Engineering*, *136*(3), 145–155.
- Heller, V., & Spinneken, J. (2013). Improved landslide-tsunami prediction: Effects of block model parameters and slide model. *Journal of Geophysical Research: Oceans*, *118*, 1489–1507. <https://doi.org/10.1002/jgrc.20099>
- Heller, V., & Spinneken, J. (2015). On the effect of the water body geometry on landslide–tsunamis: Physical insight from laboratory tests and 2D to 3D wave parameter transformation. *Coastal Engineering*, *104*, 113–134.
- Higuera, P., Lara, J. L., & Losada, I. J. (2013a). Realistic wave generation and active wave absorption for Navier–Stokes models: Application to OpenFOAM®. *Coastal Engineering*, *71*, 102–118.
- Higuera, P., Lara, J. L., & Losada, I. J. (2013b). Simulating coastal engineering processes with OpenFOAM®. *Coastal Engineering*, *71*, 119–134.
- Higuera, P., Lara, J. L., & Losada, I. J. (2014a). Three-dimensional interaction of waves and porous coastal structures using OpenFOAM®. Part I: Formulation and validation. *Coastal Engineering*, *83*, 243–258.
- Higuera, P., Lara, J. L., & Losada, I. J. (2014b). Three-dimensional interaction of waves and porous coastal structures using OpenFOAM®. Part II: Application. *Coastal Engineering*, *83*, 259–270.
- Jacobsen, N. G., van Gent, M. R., Capel, A., & Borsboom, M. (2018). Numerical prediction of integrated wave loads on crest walls on top of rubble mound structures. *Coastal Engineering*, *142*, 110–124.
- Jacobsen, N. G., van Gent, M. R., & Wolters, G. (2015). Numerical analysis of the interaction of irregular waves with two dimensional permeable coastal structures. *Coastal Engineering*, *102*, 13–29.
- Janin, A., Rodriguez, M., Sakellariou, D., Lykousis, V., & Gorini, C. (2019). Tsunamigenic potential of a Holocene submarine landslide along the North Anatolian Fault (Northern Aegean Sea, off Thasos Island): Insights from numerical modelling. *Natural Hazards & Earth System Sciences*, *19*(1), 121–136.
- Jasak, H. (1996). Error analysis and estimation for the finite volume method with applications to fluid flows (Ph.D thesis), Imperial College London (University of London).
- Jasak, H., Rigler, D., & Tuković, Ž. (2014). Design and implementation of immersed boundary method with discrete forcing approach for boundary conditions. In *11th World Congress on Computational Mechanics, WCCM 2014, 5th European Conference on Computational Mechanics, ECCM 2014 and 6th European Conference on Computational Fluid Dynamics, ECFD 2014* (pp. 5319–5332).
- Jensen, B., Jacobsen, N. G., & Christensen, E. D. (2014). Investigations on the porous media equations and resistance coefficients for coastal structures. *Coastal Engineering*, *84*, 56–72.
- Kim, J., Løvholt, F., Issler, D., & Forsberg, C. F. (2019). Landslide material control on tsunami genesis—The Storegga slide and tsunami (8,100 years BP). *Journal of Geophysical Research: Oceans*, *124*, 3607–3627. <https://doi.org/10.1029/2018JC014893>
- Koh, H. L., Tan, W. K., Teh, S. Y., & Chai, M. F. (2016). Simulation of potentially catastrophic landslide tsunami in North West Borneo Trough. *International Journal of Environmental Science and Development*, *7*(12), 889.
- Lara, J. L., del Jesus, M., & Losada, I. J. (2012). Three-dimensional interaction of waves and porous coastal structures: Part II: Experimental validation. *Coastal Engineering*, *64*, 26–46.
- Lara, J. L., Losada, I. J., Maza, M., & Guancho, R. (2011). Breaking solitary wave evolution over a porous underwater step. *Coastal Engineering*, *58*(9), 837–850.
- Lindström, E. K. (2016). Waves generated by subaerial slides with various porosities. *Coastal Engineering*, *116*, 170–179.
- Liu, P. F., Wu, T. R., Raichlen, F., Synolakis, C., & Borrero, J. (2005). Runup and rundown generated by three-dimensional sliding masses. *Journal of Fluid Mechanics*, *536*, 107–144.
- Losada, I. J., Lara, J. L., & del Jesus, M. (2016). Modeling the interaction of water waves with porous coastal structures. *Journal of Waterway, Port, Coastal, and Ocean Engineering*, *142*(6), 03116003. [https://doi.org/10.1061/\(ASCE\)WW.1943-5460.0000361](https://doi.org/10.1061/(ASCE)WW.1943-5460.0000361)
- Løvholt, F., Harbitz, C. B., & Haugen, K. B. (2005). A parametric study of tsunamis generated by submarine slides in the Ormen Lange/Storegga area off western Norway. In *Ormen Lange—an Integrated Study for Safe Field Development in the Storegga Submarine Area* (pp. 219–231). Elsevier.
- Løvholt, F., Pedersen, G., Harbitz, C. B., Glimsdal, S., & Kim, J. (2015). On the characteristics of landslide tsunamis. *Philosophical Transactions of the Royal Society A: Mathematical, Physical and Engineering Sciences*, *373*(2053), 20140376.

- Lynett, P., & Liu, P. L. F. (2005). A numerical study of the run-up generated by three-dimensional landslides. *Journal of Geophysical Research*, *110*, C03006. <https://doi.org/10.1029/2004JC002443>
- Ma, Z., Qian, L., Martinez-Ferrer, P., Causon, D., Mingham, C., & Bai, W. (2018). An overset mesh based multiphase flow solver for water entry problems. *Computers & Fluids*, *172*, 689–705.
- Marschall, H., Hinterberger, K., Schüller, C., Habla, F., & Hinrichsen, O. (2012). Numerical simulation of species transfer across fluid interfaces in free-surface flows using OpenFOAM. *Chemical Engineering Science*, *78*, 111–127.
- McFall, B. C., & Fritz, H. M. (2016). Physical modelling of tsunamis generated by three-dimensional deformable granular landslides on planar and conical island slopes. *Proceedings of the Royal Society of London. Series A: Mathematical, Physical and Engineering Sciences*, *472*(2188), 20160052.
- Miller, G. S., Take, W. A., Mulligan, R. P., & McDougall, S. (2017). Tsunamis generated by long and thin granular landslides in a large flume. *Journal of Geophysical Research: Oceans*, *122*, 653–668. <https://doi.org/10.1002/2016JC012177>
- Mohammed, F., & Fritz, H. M. (2012). Physical modeling of tsunamis generated by three-dimensional deformable granular landslides. *Journal of Geophysical Research*, *117*, C11015. <https://doi.org/10.1029/2011JC007850>
- Montagna, F., Bellotti, G., & Di Risio, M. (2011). 3D numerical modeling of landslide-generated tsunamis around a conical island. *Natural Hazards*, *58*(1), 591–608.
- Mulligan, R. P., & Take, W. A. (2017). On the transfer of momentum from a granular landslide to a water wave. *Coastal Engineering*, *125*, 16–22.
- Najafi-Jilani, A., & Ataie-Ashtiani, B. (2008). Estimation of near-field characteristics of tsunami generation by submarine landslide. *Ocean Engineering*, *35*(5-6), 545–557.
- Panizzo, A., De Girolamo, P., Di Risio, M., Maistri, A., & Petaccia, A. (2005). Great landslide events in Italian artificial reservoirs. *Natural Hazards and Earth System Sciences*, *5*(5), 733–740. <https://doi.org/10.5194/nhess-5-733-2005>
- Pelinovsky, E., & Poplavsky, A. (1996). Simplified model of tsunami generation by submarine landslides. *Physics and Chemistry of The Earth*, *21*(1-2), 13–17.
- Romano, A., Bellotti, G., & Di Risio, M. (2013). Wavenumber–frequency analysis of the landslide-generated tsunamis at a conical island. *Coastal Engineering*, *81*, 32–43.
- Romano, A., Di Risio, M., Bellotti, G., Molfetta, M., Damiani, L., & De Girolamo, P. (2016). Tsunamis generated by landslides at the coast of conical islands: Experimental benchmark dataset for mathematical model validation. *Landslides*, *13*(6), 1379–1393.
- Romano, A., Di Risio, M., Molfetta, M. G., Bellotti, G., Pasquali, D., Sammarco, P., et al. (2017). 3D physical modeling of tsunamis generated by submerged landslides at a conical island: The role of initial acceleration. *Coastal Engineering Proceedings*, *35*, 14.
- Ruffini, G., Heller, V., & Briganti, R. (2019). Numerical modelling of landslide-tsunami propagation in a wide range of idealised water body geometries. *Coastal Engineering*, *153*, 103518.
- Shi, C., An, Y., Wu, Q., Liu, Q., & Cao, Z. (2016). Numerical simulation of landslide-generated waves using a soil–water coupling smoothed particle hydrodynamics model. *Advances in Water Resources*, *92*, 130–141.
- Si, P., Shi, H., & Yu, X. (2018). A general numerical model for surface waves generated by granular material intruding into a water body. *Coastal Engineering*, *142*, 42–51.
- Sue, L., Nokes, R., & Davidson, M. (2011). Tsunami generation by submarine landslides: Comparison of physical and numerical models. *Environmental Fluid Mechanics*, *11*(2), 133–165.
- Synolakis, C. E., Bardet, J. P., Borrero, J. C., Davies, H. L., Okal, E. A., Silver, E. A., et al. (2002). The slump origin of the 1998 Papua New Guinea tsunami. *Proceedings of the Royal Society of London. Series A: Mathematical, Physical and Engineering Sciences*, *458*(2020), 763–789.
- Tang, G., Lu, L., Teng, Y., Zhang, Z., & Xie, Z. (2018). Impulse waves generated by subaerial landslides of combined block mass and granular material. *Coastal Engineering*, *141*, 68–85.
- Tinti, S., & Bortolucci, E. (2000). Energy of water waves induced by submarine landslides. *Pure and Applied Geophysics*, *157*(3), 281–318.
- Tinti, S., Manucci, A., Pagnoni, G., Armigliato, A., & Zaniboni, F. (2005). The 30 December 2002 landslide-induced tsunamis in Stromboli: Sequence of the events reconstructed from the eyewitness accounts. *Natural Hazards and Earth System Sciences*, *5*(6), 763–775.
- Van Gent, M. R. A. (1995). Wave interaction with permeable coastal structures (Ph.D thesis). Delft University.
- Veveakis, E., Vardoulakis, I., & Di Toro, G. (2007). Thermoporoelasticity of creeping landslides: The 1963 Vaiont slide, northern Italy. *Journal of Geophysical Research*, *112*, F03026. <https://doi.org/10.1029/2006JF000702>
- Viroulet, S., Sauret, A., & Kimmoun, O. (2014). Tsunami generated by a granular collapse down a rough inclined plane. *Europhysics Letters*, *105*(3), 34,004.
- Watts, P. (1998). Wavemaker curves for tsunamis generated by underwater landslides. *Journal of Waterway, Port, Coastal, and Ocean Engineering*, *124*(3), 127–137. [https://doi.org/10.1061/\(ASCE\)0733-950X\(1998\)124:3\(127\)](https://doi.org/10.1061/(ASCE)0733-950X(1998)124:3(127))
- Watts, P., Grilli, S., Kirby, J., Fryer, G., & Tappin, D. (2003). Landslide tsunami case studies using a Boussinesq model and a fully nonlinear tsunami generation model. *Natural Hazards And Earth System Sciences*, *3*(5), 391–402.
- Watts, P., Grilli, S., Tappin, D., & Fryer, G. (2005). Tsunami generation by submarine mass failure. II: Predictive equations and case studies. *Journal of Waterway, Port, Coastal, and Ocean Engineering*, *131*(6), 298–310. [https://doi.org/10.1061/\(ASCE\)0733-950X\(2005\)131:6\(298\)](https://doi.org/10.1061/(ASCE)0733-950X(2005)131:6(298))
- Weller, H. G. (2008). A new approach to VOF-based interface capturing methods for incompressible and compressible flow. *OpenCFD Ltd., Report TR/HGW, 4*.
- Whittaker, C., Nokes, R., Lo, H. Y., Liu, P. F., & Davidson, M. (2017). Physical and numerical modelling of tsunami generation by a moving obstacle at the bottom boundary. *Environmental Fluid Mechanics*, *17*(5), 929–958.
- Windt, C., Davidson, J., Akram, B., & Ringwood, J. V. (2018). Performance assessment of the overset grid method for numerical wave tank experiments in the OpenFOAM environment. In *ASME 2018 37th International Conference on Ocean, Offshore and Arctic Engineering* (pp. V010T09A006–V010T09A006).
- Yavari-Ramshe, S., & Ataie-Ashtiani, B. (2016). Numerical modeling of subaerial and submarine landslide-generated tsunami waves recent advances and future challenges. *Landslides*, *13*(6), 1325–1368.
- Zitti, G., Ancy, C., Postacchini, M., & Brocchini, M. (2016). Impulse waves generated by snow avalanches: Momentum and energy transfer to a water body. *Journal of Geophysical Research: Earth Surface*, *121*, 2399–2423. <https://doi.org/10.1002/2016JF003891>